Inorganic Chemistry

Article

pubs.acs.org/IC

Redox Noninnocence of the Bridge in Copper(II) Salophen and Bis(oxamato) Complexes

David de Bellefeuille,[†] Maylis Orio,[‡] Anne-Laure Barra,[§] Ally Aukauloo,[∥,⊥] Yves Journaux,[∥,#] Christian Philouze,[▽] Xavier Ottenwaelder,*[,†] and Fabrice Thomas*[,▽]

[†]Department of Chemistry and Biochemistry, Concordia University, Montreal, Quebec H4B 1R6, Canada

[‡]Laboratoire de Spectrochimie Infrarouge et Raman, Université des Sciences et Technologies de Lille, UMR CNRS 8516, 59655 Villeneuve d'Ascq Cedex, France

[§]Laboratoire National des Champs Magnétiques Intenses, CNRS, 25 rue des Martyrs, 38042 Grenoble, France

[∥]Institut de Chimie Moléculaire et des Matériaux d'Orsay, UMR CNRS 8182, Université Paris-Sud XI, 91405 Orsay, France

[⊥]Service de Bioénergétique, Biologie Structurale et Mécanismes (SB2SM), CEA, iBiTec-S; Biochimie Biophysique et Biologie Structurale (B3S), I2BC, UMR 9198, 91191 Gif-sur-Yvette, France

[#]Sorbonne Universités, UPMC Université Paris 06, UMR CNRS 8232, Institut Parisien de Chimie Moléculaire, France

[▽]Equipe CIRE, Département de Chimie Moléculaire, UMR CNRS 5250, Université Grenoble-Alpes, 38041 Grenoble Cedex 9, France

Supporting Information

ABSTRACT: Two square-planar copper(II) complexes of 1,2-bis(2-hydroxy-3,5-di-*tert*-butylbenzimino)-4,5-bis-(dimethylamino)benzene (**1**) and *N*-[4,5-bis(dimethylamino)-2-(oxalylamino)benzene]oxamate ($\mathbf{2}^{2-}$) were prepared. The crystal structures of the proligands $H_2\mathbf{L}^1$ and $Et_2H_2\mathbf{L}^2$, as well as the corresponding complexes, are reported. The proligands each display a one-electron-oxidation wave, which is assigned to oxidation of the bis(dimethylamino)benzene moiety into a π radical. Complexes **1** and $\mathbf{2}^{2-}$ exhibit reversible one-electron-oxidation waves in their cyclic voltammograms ($E_{1/2}{}^1 = 0.14$ and $E_{1/2}{}^2 = 0.31$ V for **1** and $E_{1/2}{}^1 = -0.47$ V vs Fc^+/Fc for $\mathbf{2}^{2-}$). The first process corresponds to oxidation of the bis(dimethylamino)benzene central ring into a π radical, while the second process for **1** is ascribed to oxidation of the π radical into an α-diiminoquinone. The one-electron-oxidized species $\mathbf{1}^+$ and $\mathbf{2}^-$ exhibit intense visible−near-IR absorptions, which are diagnostic of π radicals. They display a triplet signal in their electron paramagnetic resonance spectra, which stem from magnetic coupling between the ligand-radical spin and the copper(II) spin. The zero-field-splitting parameters are larger for $\mathbf{2}^-$ than $\mathbf{1}^+$ because of greater delocalization of the spin density onto the coordinated amidato N atoms. Density functional theory calculations support a π-radical nature of the one-electron-oxidized complexes, as well as $S = 1$ ground spin states. The electrogenerated $\mathbf{1}^{2+}$ comprises a closed-shell diiminoquinone ligand coordinated to a copper(II) metal center. Both **1** and **2** catalyze the aerobic oxidation of benzyl alcohol, albeit with different yields.

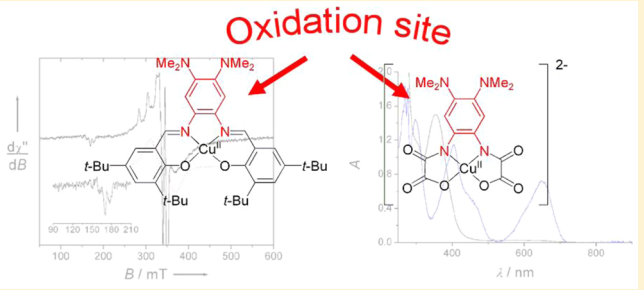

1. INTRODUCTION

The coordination chemistry of d-transition-metal complexes with redox-noninnocent ligands currently attracts considerable interest. A radical ligand not only imparts unique electronic properties to the complex but also profoundly tunes its catalytic activity.[1] Many examples of cooperativity between a metal ion and an organic radical moiety during turnover exist in biology (galactose oxidase,[2] cytochrome P450,[3a−d] and ribonucleotide reductase[4]), with the most prevalent biological radical cofactors being both tyrosyl[2] and one-electron-oxidized hemes.[3] A number of synthetic ligands are believed to be redox-noninnocent when engaged within a complex.[5] The most representative ones are porphyrins,[6] phenolates,[7] catecholates,[8] aminophenolates,[9] phenylenediamines,[10] α-diimines,[11] and dithiolenes.[12] In principle, one-electron oxidation of a M^{n+}−L complex, wherein the ligand L is suspected to be redox-noninnocent, affords the high-valent $M^{(n+1)+}$−L species or the radical M^{n+}−$L^\bullet$ electromer or an equilibrium of both (valence tautomerism). The electronics of the ligand, the size of the chelate ring, and the nature of the metal ion are crucial factors that govern the oxidation site. This intricacy is illustrated by recent investigations on copper salen complexes (Scheme 1). Oxidation of $[Cu^{II}(Salcn^{tBu})]$ indeed affords a copper(II)

Received: June 8, 2015
Published: September 4, 2015

DOI: 10.1021/acs.inorgchem.5b01285
Inorg. Chem. 2015, 54, 9013−9026

Scheme 1. Electronic Structure of One-Electron-Oxidized Copper(II) Salen Complexes: (a) $[Cu^{II}(Salcn^{tBu})]$;[13] (b) $[Cu^{II}(Salcn^{OMe})]$;[14] (c) $[Cu^{II}(Sal\text{-}1,3\text{-}cn^{tBu})]$[15]

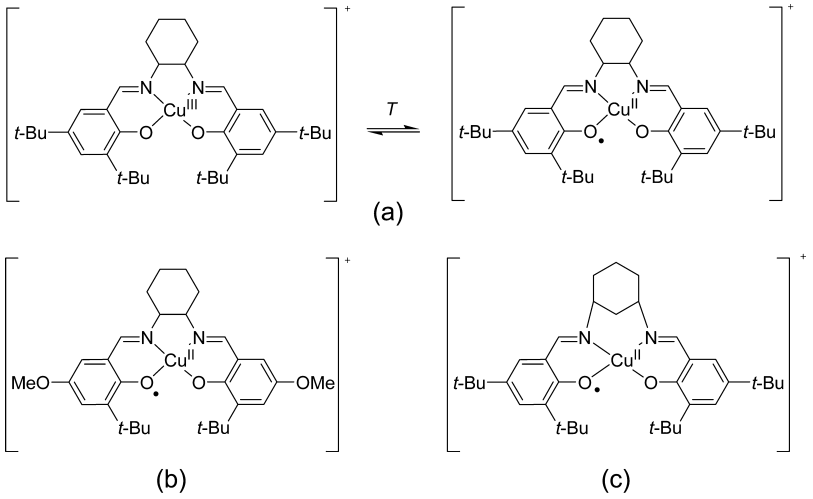

Scheme 2. Formulas of Complexes (a) $[Ni(L^1)]^+$,[16] (b) $[Ni(L^2)]^-$,[17] and (c) $[Cu^{III}opba]^-$[18]

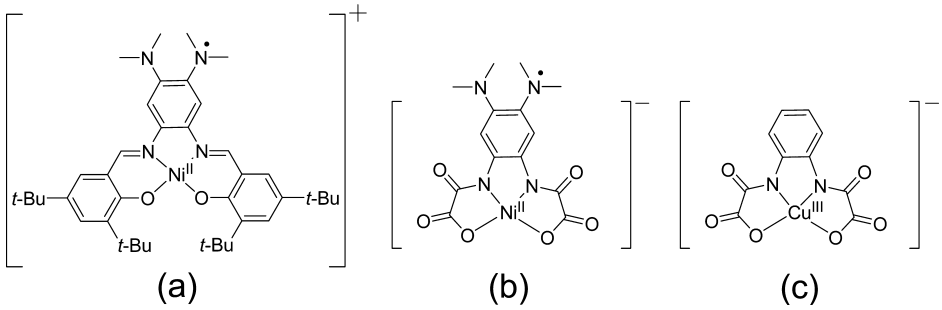

radical complex in thermal equilibrium with the copper(III) phenolate species.[13] In contrast, single-electron oxidation of $[Cu^{II}(Salcn^{OMe})]$[14] and $[Cu^{II}(Sal\text{-}1,3\text{-}cn^{tBu})]$[15] affords the copper(II) phenoxyl radical electronic isomer, irrespective of the temperature. Further, the extent of ligand-radical delocalization was shown to be temperature-dependent in the copper salophen family, wherein delocalization on the whole aromatic framework prevails at high temperatures. The shift in the oxidation site from ligand to metal and alternatively from one ligand site to another one not only affects the spectroscopic properties but also the reactivity and stability of the oxidized species.

In a previous paper, we reported on the redox properties of the nickel(II) salophen complex $[Ni^{II}(\mathbf{L^1})]$ (Scheme 2a), whose bridging ring contains strongly electron-donating dimethylamino substituents.[16] We established that $[Ni^{II}(\mathbf{L^1})]$ undergoes two reversible one-electron transfers centered on the diaminobenzene ring. The nickel(II) bis(oxamato) complex $[Ni^{II}(\mathbf{L^2})]^{2-}$ (Scheme 2b), which has been described earlier, also exhibits a redox activity centered on the diaminobenzene ring, affording a nickel(II) π-radical complex.[17] This result was striking because both the nickel(II)[17] and copper(II)[18] complexes of the related bis(oxamato) unsubstituted ligand undergo metal-centered redox activity (Scheme 2c). Because the redox-active orbitals of the copper are expected to be closer in energy to the ligand than the nickel ones and oxidation of copper(II) into copper(III) can occur without a change in the coordination number, we were interested in investigating the oxidative redox chemistry of the copper complexes $[Cu^{II}(\mathbf{L^1})]$ (**1**) and $[Cu^{II}(\mathbf{L^2})]^{2-}$ ($\mathbf{2^{2-}}$). By spectroelectrochemistry, electron paramagnetic resonance (EPR), and density functional theory (DFT) calculations, we establish that one-electron oxidation of **1** and $\mathbf{2^{2-}}$ affords copper(II) π-cation-radical complexes of very similar nature. Because the copper radical species can be considered as mimics of the galactose oxidase active site,[2] we examined the ability of **1** and $\mathbf{2^{2-}}$ to catalyze the aerobic oxidation of alcohols by using benzyl alcohol as the model substrate. Finally, we show that the two-electron oxidation of **1** produces the copper(II) complex $\mathbf{1^{2+}}$ in which the ligand adopts an α-diiminoquinone closed-shell form.

2. EXPERIMENTAL SECTION

2.1. Materials. Organics reagents, solvents, and metal salts were obtained from commercial sources and used as received unless indicated otherwise. For oxidation studies, dichloromethane was degassed, dried over a solvent purification system, and then stored over activated 4 Å molecular sieves inside an inert-atmosphere glovebox filled with a dry nitrogen atmosphere (less than 1 ppm in oxygen and water). $H_2\mathbf{L^1}$ and $Et_2H_2\mathbf{L^2}$ were prepared by literature procedures.[16,17]

2.2. Characterization. Elemental CHN microanalyses were performed by the Microanalytical Service of the Institut de Chimie des Substances Naturelles (CNRS, France). Solution ^1H and ^{13}C NMR spectra were recorded on a Varian Innova 500 MHz instrument using tetramethylsilane as the internal reference. UV−vis−near-IR (NIR) solution spectra were recorded on Varian Cary 5E and PerkinElmer Lambda 1050 spectrophotometers. X-band EPR spectra were recorded on a Bruker EMX Plus spectrometer controlled with *Xenon* software and equipped with a Bruker teslameter. A Bruker nitrogen-flow cryostat connected to a high-sensitivity resonant cavity

DOI: 10.1021/acs.inorgchem.5b01285
Inorg. Chem. 2015, 54, 9013−9026

was used for 293 and 100 K measurements. An Oxford Instrument helium-flow cryostat connected to a dual-mode resonant cavity was used to run experiments at 25 K. High-frequency EPR measurements were performed on a multifrequency spectrometer operating in a double-pass configuration. The main magnetic field was provided by a 16 T superconducting magnet. Frequencies were generated with the help of multipliers (doubler or tripler) associated with a PDRO frequency source. The EPR signal was detected with a hot electron InSb bolometer.[19] The spectra were simulated using *SIMFONIA* software (Bruker). Cyclic voltammetry (CV) curves were recorded on a CHI 620 potentiostat in a standard three-electrode cell under an argon atmosphere. Electrochemical measurements were performed at either 298 K for the nonoxidized complexes or 233 K for the oxidized species to ensure as little decomposition as possible. An $AgNO_3/Ag$ (0.01 M) reference electrode was used. All of the potentials given in the text refer to the regular Fc^+/Fc redox couple used as the external reference. A platinum disk (1 mm diameter) polished with 1 μm diamond paste was used as the working electrode for CV experiments. Electrolysis experiments were conducted at 233 K under argon by using a Bio-Logic SP300 potentiostat, using a platinum grid (2 cm × 2 cm) as the working electrode. The electrolysis was monitored by both coulometry and rotating-disk-electrode (RDE) voltametry. For the catalytic experiments, benzaldehyde was quantified by gas chromatography (Shimadzu GC-17A). The solution, which contains biphenyl as an internal standard, was passed through a Celite column before analysis. For experiments under 2 bar of dioxygen, we used a HEL high-pressure ChemSCAN reactor.

2.3. X-ray Crystallography. Crystallographic analysis was performed on a Bruker APEX-DUO diffractometer or on a Kappa CCD Nonius diffractometer. The frames were integrated with the Bruker *SAINT* software package using a narrow-frame algorithm. Data were corrected for absorption effects using the multiscan method (*SADABS*). The structures were solved by direct methods and refined using the *APEX2* or *OLEX2* software packages (*SHELXL* instructions).[20] All non-H atoms were refined with anisotropic thermal parameters. H atoms were generated in idealized positions, riding on the carrier atoms with isotropic thermal parameters.

2.4. Computational Details. All theoretical calculations were performed with the *ORCA* program package.[21] Full geometry optimizations were carried out for all complexes using the GGA functional BP86[22−24] in combination with the TZV/P[25] basis set for all atoms and by taking advantage of the resolution of the identity (RI) approximation in the Split-RI-J variant[26] with the appropriate Coulomb fitting sets.[27] Increased integration grids (Grid4 in the *ORCA* convention) and tight self-consistent-field (SCF) convergence criteria were used. Solvent effects were accounted for according to the experimental conditions. For that purpose, we used the CH_2Cl_2 (ε = 9.08) solvent within the framework of the conductor-like screening (COSMO) dielectric continuum approach.[28] The relative energies were obtained from single-point calculations using the B3LYP[29,30] functional together with the TZV/P basis set. They were computed from the gas-phase-optimized structures as a sum of the electronic energy, thermal corrections to free energy, and free energy of solvation. The optical properties were predicted from additional single-point calculations using the same functional/basis set as those employed before. Electronic transition energies and dipole moments for all models were calculated using time-dependent DFT (TD-DFT)[31−33] within the Tamm−Dancoff approximation.[34,35] To increase the computational efficiency, the RI approximation[36] was used in calculating the Coulomb term, and at least 30 excited states were calculated in each case. **g** tensors and hyperfine coupling (hfc) constants[36−39] were obtained from single-point calculations using the B3LYP functional. The EPR-II[40] basis set was employed for the ligands, while scalar relativistic effects accounted for the metal complexes. They were included with ZORA paired with the SARC def2-TZVP(-f) basis sets[41,42] and the decontracted def2-TZVP/J Coulomb fitting basis sets for all atoms. Increased integration grids (Grid4 and GridX4 in the *ORCA* convention) and tight SCF convergence criteria were used in the calculation. The integration grids were increased to an integration accuracy of 11 (*ORCA* convention) for the metal center. Picture change effects were applied for calculation of the hyperfine tensors. The Heisenberg isotropic exchange coupling constants J were evaluated from single-point calculations based on the broken-symmetry (BS) approach[43−45] using the B3LYP functional and TZV/P basis set. The Yamaguchi formula[46,47] was used to estimate the exchange coupling constants J based on the Heisenberg−Dirac−van Vleck Hamiltonian: $H = -2JS_1S_2$.[48−51] Zero-field-splitting (ZFS) parameters were obtained from ab initio calculations based on the complete active-space self-consistent-field (CASSCF) approach. The spin−orbit coupling (SOC) was calculated within a quasi-degenerate perturbation theory formalism, where the SOC operator is diagonalized on the basis of multiconfigurational wave functions obtained from a full configuration-interaction (CI) calculation in a limited set of active electrons and orbitals that were obtained from a preceding CASSCF calculation.[52] The active space was chosen to consist of 12 active electrons occupying the five 3d-based molecular orbitals (MOs) and two ligand π orbitals [CAS(12,7)]. The CASSCF calculations were performed using the TZV/P basis set and were converged for the average of 10 triplet and 10 singlet roots. The SOC matrix was diagonalized on the basis of all possible triplet (21) and singlet (28) states. The spin−spin (SS) contribution to the ZFS was calculated on the basis of a single-root CAS(12,7) wave function.[52]

2.5. Synthesis. ***1***. To a solution of $H_2\mathbf{L}^1$ (313 mg, 0.5 mmol) in CH_2Cl_2 (5 mL) was added dropwise a solution of $Cu(OAc)_2{\cdot}H_2O$ (200 mg, 1.0 mmol) in MeOH (15 mL). After 2 h of mild reflux, the solvent was evaporated in vacuo and the crude was solubilized in fresh CH_2Cl_2 (50 mL). This solution was filtered over a SiO_2 pad to remove excess metal, and the filtrate was evaporated until concentrated. After layering with MeOH and cooling to −20 °C, the precipitate was collected by filtration as a burgundy/brown solid, complex **1**. Yield: 120 mg, 35%. $R_f(SiO_2/CH_2Cl_2)$: 0.81. Anal. Calcd for $C_{40}H_{56}CuN_4O_2$ (688.44 g mol^{-1}): C, 69.78; H, 8.20; N, 8.14. Found: C, 69.16; H, 8.10; N, 8.02. IR σ (cm^{-1}): 1585 (imine), 1605 (imine). Single crystals of **1** were grown by the slow evaporation of a concentrated CH_2Cl_2 solution at 25 °C.

*$[PPh_4]_2$**2**$\cdot 2H_2O$.* Under an inert atmosphere, $Et_2H_2\mathbf{L}^2$ (150 mg, 0.38 mmol) and 4.25 equiv of NaOH (65 mg, 1.62 mmol) were dissolved in 10 mL of degassed water. A degassed solution of $Cu(NO_3)_2{\cdot}3H_2O$ (92 mg, 0.38 mmol) in water (20 mL) was added very slowly (1 drop s^{-1}) to the ligand solution under vigorous stirring. The mixture was left to stir under nitrogen for 15 min after the last drop and then transferred in air to a separatory funnel. The complex was extracted portionwise by the following procedure: adding 50 mL of CH_2Cl_2 and a portion of PPh_4Cl and then mixing and separating the organic phase. This procedure was repeated until 2 equiv of PPh_4Cl was added or while the organic phase remained deeply colored. The combined organic phases were filtered over paper and evaporated to dryness. The crude was triturated for 1 h in acetone, filtered off, then triturated again in acetone overnight. The green solid of $[PPh_4]_2$**2**$\cdot 2H_2O$ was collected by filtration, washed with acetone, and dried in vacuo. Yield: 197 mg, 35%. Anal. Calcd for $C_{14}H_{14}CuN_4O_6{\cdot}2H_2O$ (1112.64 g mol^{-1}): C, 66.93; H, 5.25; N, 5.04. Found: C, 67.67; H, 5.22; N, 4.89. IR σ (cm^{-1}): 1688 (C═O amide), 1731 and 1748 (C═O ester). Purple/green birefringent single crystals of $[PPh_4]_2$**2** were grown by vapor diffusion of acetone into a concentrated CH_3CN solution of the complex.

3. RESULTS AND DISCUSSION

3.1. Synthesis. The proligands $H_2\mathbf{L}^1$ and $Et_2H_2\mathbf{L}^2$ were synthesized according to published procedures.[16,17] Complex **1** was formed by the reaction of $H_2\mathbf{L}^1$ with copper(II) acetate, whereby coordination occurs upon deprotonation of the phenolate by the acetate ions (Scheme 3). In the case of $Et_2H_2\mathbf{L}^2$, saponification with aqueous sodium hydroxide is required prior to slow addition of the copper(II) salt. The doubly negatively charged complex is then isolated by ion

DOI: 10.1021/acs.inorgchem.5b01285
Inorg. Chem. 2015, 54, 9013−9026

Scheme 3. Proligands (H_2L^1 and $Et_2H_2L^2$) and Copper(II) Complexes Investigated in This Work: 1 and 2^{2-} as a PPh_4^+ Salt

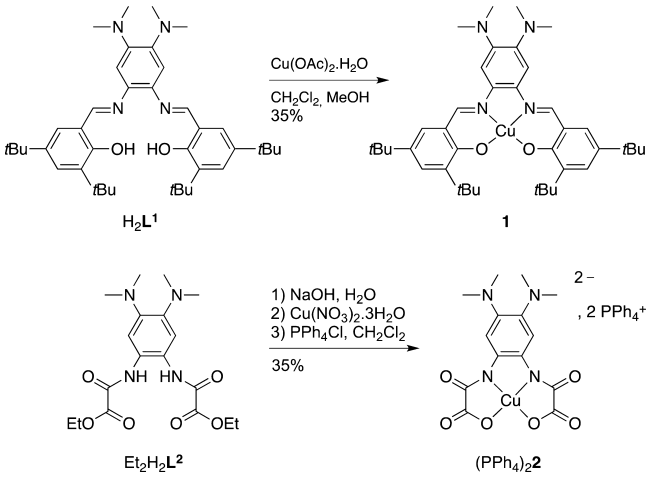

metathesis as its PPh_4^+ salt, which confers upon 2^{2-} greater solubility in organic solvents such as CH_2Cl_2 or CH_3CN.

The proligands and complexes were characterized by X-ray crystallography (Figures 1 and S1 and Table S1). The three

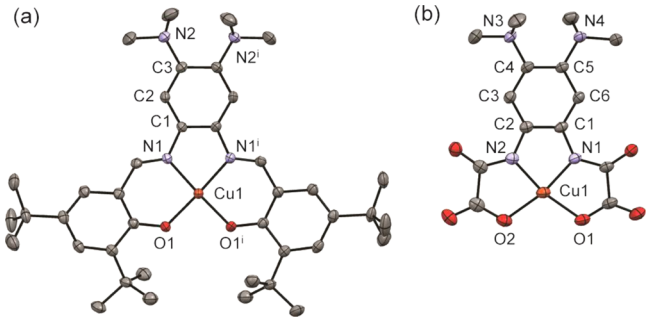

Figure 1. ORTEP representation at 50% ellipsoid probability of the complexes, with selected bond lengths (Å). H atoms are omitted for clarity, except those engaged in hydrogen bonding. (a) **1** (i: $x, y, 0.5 - z$): Cu1−O1, 1.8922(16); Cu1−N1, 1.9349(19); (b) the anion in $[PPh_4]_2$**2**: Cu1−O1, 1.9490(14); Cu1−O2, 1.9609(14); Cu1−N1, 1.9122(16); Cu1−N2, 1.8958(16).

aromatic rings in H_2L^1 are noncoplanar, allowing for the establishment of hydrogen bonds between the hydroxyl H atoms and the adjacent imine N atoms. In the case of $Et_2H_2L^2$, only one intramolecular hydrogen bond is present, between N2−H of one amide and O1 of the opposite amide. Intermolecular hydrogen bonds are also found between N1−H and the carbonyl of a second ligand molecule, as well as between the carbonyl O2 and the N−H donor of another ligand molecule. Complex **1** is isostructural to its nickel(II) analogue previously reported.[16] Both **1** and 2^{2-} exhibit a square-planar copper(II) coordination geometry that is typical for salophen and bis(oxamato) environments.[53,54] Although the entire molecule of **1** is puckered, with a 30° angle between the mean phenolate planes, the angle between the two N−Cu−O planes is only 5°. In 2^{2-}, this angle is less than 1°, but the Cu−O bonds are longer because of the 5−5−5 chelate arrangement. The 6−5−6 chelate sequence in **1** provides a geometry closer to strict square-planar.

In all proligands and complexes, one methyl of each NMe_2 group is significantly out of planarity with the central aromatic ring ($C_{arom}-C_{arom}-N-C_{Me}$ torsion angles between 56 and 70°). The steric clash between methyl groups enforces the nitrogen lone pair of the NMe_2 substituents to tilt out of the plane of the aromatic ring. The sum of the C−N−C angles about the NMe_2 substituents ranges from 338° to 347°, indicating intermediate hybridization between sp^2 and sp^3. Resonance with the NMe_2 groups is thus limited.

3.2. Oxidation of H_2L^1 and $Et_2H_2L^2$. The electrochemical behavior of the proligands H_2L^1 and $Et_2H_2L^2$ was studied in CH_2Cl_2 (+0.1 M nBu_4NClO_4 as the supporting electrolyte). The cyclic voltammogram of H_2L^1 displays two oxidation waves at $E_{1/2}{}^1 = 0.07$ V ($\Delta E_p = 0.06$ V) and $E_{1/2}{}^2 = 0.25$ V versus the Fc^+/Fc couple (Figure S2 and Table 1). While the first redox transfer is reversible, the low $I_p{}^a/I_p{}^c$ value for the second wave indicates that the dication is poorly stable. The $E_{1/2}{}^1$ and $E_{1/2}{}^2$ values are within the range of those measured for the oxidation of a series of poly(dimethylamino) aromatic derivatives,[55−57] suggesting sequential oxidations of the central tetraaminobenzene ring into a radical cation and then a closed-shell α-diiminoquinone dication. It is worth noting that oxidation of the parent salophen ligand that is unsubstituted on the central ring occurs at higher potentials in a proton-coupled electron-transfer mechanism, affording a hydrogen-bonded iminium phenoxyl system.[53a] The strong electron-donating effect of the NMe_2 groups in H_2L^1 makes the central tetraaminobenzene ring easier to oxidize and shifts the first oxidation site from phenol to the central tetraaminobenzene ring. Coulometric measurements at a fixed potential of 0.1 V establish that the first redox wave corresponds to a one-electron transfer and that the cation $(H_2L^1)^+$ is stable at the time scale of electrolysis (30 min at 233 K). This was not the case for the dication, which

Table 1. Redox Potentials[a]

	$E_{1/2}{}^1$	$I_p{}^a/I_p{}^{c,1}$	$E_{1/2}{}^2$	$I_p{}^a/I_p{}^{c,2}$	$E_{1/2}{}^3$	$I_p{}^a/I_p{}^{c,3}$	$E_{1/2}{}^4$
H_2L^1	0.07 (60)		0.25[b]				
$Et_2H_2L^2$	0.24, −0.07[c]						
1[d]	0.09 (60)	1.11	0.22 (60)	3.04	0.82 (80)	2.25	0.96 (irr)
NiL^1[e]	0.12		0.24		0.97		
$1H^+$	0.62, 0.28[c]	1.27					
2^{2-}	−0.47 (80)	1.59	−0.17[f]				
$(NiL^2)^{2-}$[g]	−0.51						

[a]In volts versus the Fc^+/Fc couple. Conditions: 1.0 mM sample in CH_2Cl_2 + 0.1 M nBu_4NClO_4; $T = 293$ K. The peak-to-peak separations ΔE_p given in millivolts in parentheses. [b]Irreversible process: $E_p{}^a$ is given. [c]ECE process: $E_p{}^a$ and $E_p{}^c$ are given. [d]In nBu_4NPF_6, the oxidation potentials are 0.14 V (90), 0.31 V (110), 0.94 V (100), and 1.13 V (100). [e]Reference 16. [f]The profile and intensity of the cathodic wave suggests adsorption of **2** on the electrode; $E_p{}^a$ is given. [g]Reference 17.

DOI: 10.1021/acs.inorgchem.5b01285
Inorg. Chem. 2015, 54, 9013−9026

decomposes significantly during electrolysis. Similarly, cation $(H_2L^1)^+$ could be obtained by chemical oxidation using 1 equiv of acetylferrocenium at 233 K (Figure S4).

The CV of $Et_2H_2L^2$ exhibits an anodic peak at 0.24 V, which is associated with a cathodic one at −0.07 V (Figure S2). The large ΔE_p value (0.31 V) is consistent with an ECE mechanism, which is tentatively assigned to a reorganization of the hydrogen-bonded network. The anodic potential is 0.15 V higher than $E_{1/2}{}^1$ of H_2L^1, showing that the hydrogen-bonded amide groups exert a stronger electron-withdrawing effect than the hydrogen-bonded imines.[58] As in the case of H_2L^1, coulometric titration reveals that the oxidation wave corresponds to a one-electron transfer and that the stability of the oxidized species is noteworthy, which was also confirmed by chemical oxidation at 233 K (Figure S5).

The ligand cations $(H_2L^1)^+$ and $(Et_2H_2L^2)^+$ were prepared by exhaustive electrolysis or chemical oxidation (both gave similar results) and characterized by UV−vis and EPR spectroscopies. The UV−vis spectrum of $(H_2L^1)^+$ in CH_2Cl_2 (+0.1 M nBu_4NClO_4) contrasts sharply with that of its neutral counterpart (Figure S3a and Table 2). While H_2L^1 does not display absorption bands above 500 nm, several transitions could be detected in the visible region in the case of $(H_2L^1)^+$, mainly as shoulders at 430, 510, and 680 nm. Similarly, $Et_2H_2L^2$ does not absorb in the visible region, whereas cation $(Et_2H_2L^2)^+$ exhibits radical features at 575 nm [660 M^{-1} cm^{-1}] (Figure S3b). Related transitions were reported for free radicals of the Würster's type by Granick et al.[59] Thus, the oxidation site in $(H_2L^1)^+$ and $(Et_2H_2L^2)^+$ is likely the bridging bis(dimethylamino)benzene ring. The shift in the absorption band on going from $(H_2L^1)^+$ to $(Et_2H_2L^2)^+$ is ascribed to changes in the electron-donating ability of imine versus amide groups and the extension of the π system in $(H_2L^1)^+$. The radical nature of the cations was confirmed by EPR spectroscopy. The isotropic X-band EPR spectra of $(H_2L^1)^+$ and $(Et_2H_2L^2)^+$ in CH_2Cl_2 both display a signal centered at g = 2.003 with a well-resolved hyperfine splitting (Figure S6). The hyperfine splitting arises from the interaction of the electron spin with H and N atoms. The spectra are not superimposable, showing that the salicyl/amide substituents affect the spin distribution. It is worth mentioning that the one-electron-oxidized salophen ligand, which does not harbor any substituent on the central ring, displays a sharp isotropic resonance at g = 2.005 without hyperfine splitting.[53a] This signature was observed for several salen ligands and appears as a hallmark for an oxidation centered on the phenol group, which produces a phenoxyl radical hydrogen-bonded to an iminium proton. The hyperfine splitting observed in the case of $(H_2L^1)^+$ and $(Et_2H_2L^2)^+$ therefore points to a different oxidation site. The experimental spectrum of $(H_2L^1)^+$ could be simulated by using the spin Hamiltonian parameters A_N = 0.46 mT (two equivalent ^{14}N) and A_H = 0.64 mT (12 equivalent of ^1H). Simulation of the spectrum of $(Et_2H_2L^2)^+$ gives the following values: A_N = 0.55 mT (two equivalent ^{14}N) and A_H = 0.70 mT (12 equivalent ^1H). These hfc constants are consistent with an unpaired electron essentially shared between the two dimethylamino substituents. The hfc constants of $(H_2L^1)^+$ are slightly different from those reported for $[Ni(L^1)]^+$,[16] highlighting the influence of coordination on the spin density in the π radical. Further, the hfc constants obtained for $(Et_2H_2L^2)^+$ are larger than those measured for $(H_2L^1)^+$, indicative of a higher amount of spin on the dimethylamino substituents in $(Et_2H_2L^2)^+$. Latta and Taft established empirical relationships between the hfc constants of the N and H atoms and the σ^+ Hammett of the substituent in para-substituted *N,N*-dimethylaniline cation radicals.[60] An increase in σ^+ (i.e., a more electron-withdrawing group, which makes the compound harder to oxidize) results in higher hfc constants. Such a correlation applies here, with $(Et_2H_2L^2)^+$ being harder to oxidize and exhibiting larger hfc constants than $(H_2L^1)^+$.

DFT calculations were undertaken using the *ORCA* program package in order to gain insight into the geometric and electronic structures of proligands H_2L^1 and $Et_2H_2L^2$ and their one-electron-oxidized derivatives (Figures S7−S12). The structural rearrangements induced by the oxidation of H_2L^1 into $(H_2L^1)^+$ and $Et_2H_2L^2$ into $(Et_2H_2L^2)^+$ mainly occur in the bridging ring (Tables S2 and S3). For instance, the (N)C−C(N) bonds are elongated by 0.019−0.034 Å, while the other C−C bonds vary within −0.017 to +0.015 Å. The shortening of the $C-N_{dimethylamino}$ bonds is much more important than that of the $C-N_{imine}$ or $C-N_{amide}$ bonds, consistent with the unpaired electron residing mainly on the bis(dimethylamino) side of the bridge. Electronic structure calculations on oxidized proligands $(H_2L^1)^+$ and $(Et_2H_2L^2)^+$ indicate that the spin density is spread over the tetraminobenzene ring. Positive Mulliken spin population is indeed found at the dimethylamino N atoms and the N-adjacent aromatic C atoms, while that on the imine/amide N atoms or phenols is negligible (Figure 2).

Finally, EPR parameters of oxidized proligands $(H_2L^1)^+$ and $(Et_2H_2L^2)^+$ were calculated (Table S4). The predicted isotropic **g** tensors (2.0032 and 2.0034, respectively) are close to that of the free electron and match quite well the experimental values. An excellent agreement is also found between the experimental and calculated hfc constants for the ^{14}N and ^1H centers of the dimethylamino substituents, which is consistent with the spin density being mainly distributed over these groups.

Table 2. Electronic Transitions of the Ligands and $1^{0/+/2+}$ and $2^{2-/-}$

	experimental λ, nm (ε, mM^{-1} cm^{-1})	TD-DFT λ, nm (f)	assignment[a]
H_2L^1	361 (21.1), 410sh (16.6)		
$(H_2L^1)^+$	430sh (8.34), 510sh (3.35), 680sh (1.11)		
$Et_2H_2L^2$	274 (12.6), 320sh (10.0)		
$(Et_2H_2L^2)^+$	362 (7.44), 575 (0.66)		
1	500sh (15.5)	554 (0.229)	LMCT
	439 (38.1)	460 (0.528)	LLCT
$\mathbf{1}^+$	972 (5.60)	980 (0.132)	ILCT
	508 (30.6)	522 (0.606)	MLCT
	446 (31.4)	422 (0.615)	LLCT
	328 (29.7)	326 (0.444)	LLCT
$\mathbf{1}^{2+}$	778 (10.2)	737 (0.271)	LMCT
	486 (39.2)	518 (0.738)	ILCT
	330 (26.4)	370 (0.182)	LLCT
$\mathbf{2}^{2-}$	569 (0.270)	538 (0.028)	LMCT
	355 (14.8)	360 (0.220)	LLCT
$\mathbf{2}^-$	648 (9.47)	645 (0.207)	ILCT
	405 (14.9)	455 (0.258)	LLCT
	298 (18.8)	nd	nd

[a]See section 3.7 for more details. CT = charge transfer, LM = ligand-to-metal, ML = metal-to-ligand, IL = intraligand (two different moieties of the ligand), and LL = ligand-to-ligand (same moiety).

3.3. Spectroscopic Properties of 1, 1H$^+$, and 2^{2-}. The UV−vis spectrum of **1** in CH_2Cl_2 (Figure 3) displays a main

DOI: 10.1021/acs.inorgchem.5b01285
Inorg. Chem. 2015, 54, 9013−9026

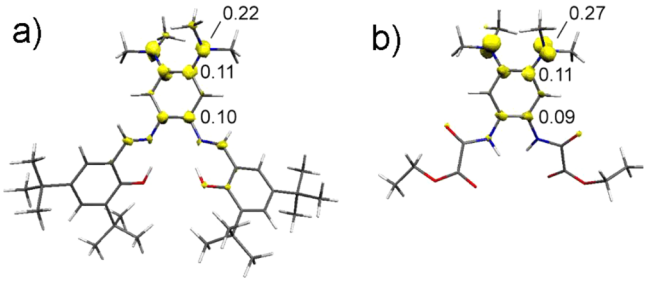

Figure 2. Spin-density plots, including the values of the most important individual spin populations for (a) $(H_2L^1)^+$ and (b) $(Et_2H_2L^2)^+$.

absorption band at 439 nm (38100 M^{-1} cm^{-1}) that is assigned to a charge-transfer (CT) transition. As expected, this band is slightly blue-shifted in comparison to the isostructural nickel complex.[16] It is close in energy to the main visible band of copper salophen complexes featuring di-*tert*-butylphenolate donors.[53] The UV−vis spectrum of $\mathbf{2}^{2-}$ consists of an intense CT band at 355 nm (14800 M^{-1} cm^{-1}). In both complexes, a low-intensity shoulder was additionally detected at around 600 nm, which is assigned to d−d transitions. Complex $\mathbf{1}H^+$ was prepared by adding 1 mol equiv of $HClO_4$ to a CH_2Cl_2 solution of **1** and subsequent stirring for 3 h. Upon protonation, the initially intense brown solution of **1** turns red-orange. The loss of intensity in the CT band (Figure S13) is consistent with protonation of one dimethylamino substituent of the bridging ring.[16] In the case of $\mathbf{2}^{2-}$, the addition of $HClO_4$ initiates precipitation of an unknown complex and has not been further investigated.

Frozen-solution X-band EPR spectra of **1**, $\mathbf{1}H^+$, and $\mathbf{2}^{2-}$ (Figures 4 and S14) reveal axial $S = {}^1/_2$ signals that are typical for square-planar copper(II) complexes.[61] The EPR spectra were simulated with the spin-Hamiltonian parameters given in Table 3. The g_3/A_3 ratio is indicative of the geometry of the metal center.[62,63] For **1**, $\mathbf{1}H^+$, and $\mathbf{2}^{2-}$, this ratio is between 101 and 106 cm, consistent with a square-planar geometry of the Cu ion. In addition, the g_3 value is smaller for $\mathbf{1}H^+$ than for **1**, reflecting a decreased ligand field in the former complex. This is a direct consequence of the protonation of one dimethylamino substituent, making the bridging moiety a weaker donor. The EPR spectrum of $\mathbf{2}^{2-}$ in frozen CH_2Cl_2 is typical for a square-planar Cu^{II} ion coordinated by strong amidato donors.[18] The superhyperfine coupling constants with four equivalent N atoms are well-resolved in both the parallel and perpendicular

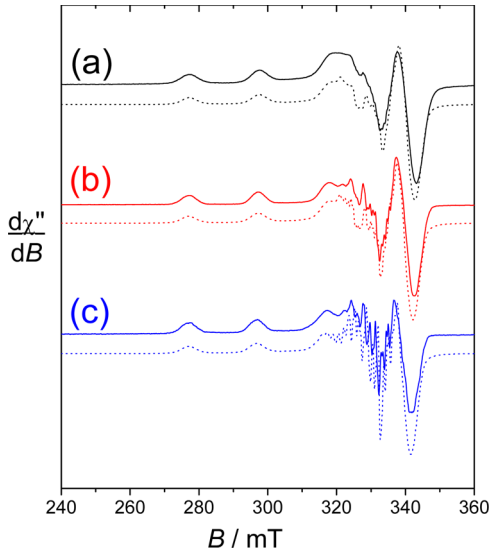

Figure 4. X-band EPR spectra of **1** (a, black), $\mathbf{1}H^+$ (b, red), and $\mathbf{1}^{2+}$ (c, blue) in a 1 mM CH_2Cl_2 frozen solution (+0.1 M nBu_4PF_6). Microwave frequency = 9.45 GHz, power = 5 mW, modulation frequency = 100 kHz, amperage = 0.3 mT, and T = 100 K. Solid lines: Experimental spectra. Dotted lines: Simulations using the parameters given in the text.

Table 3. Experimental and Calculated Spin-Hamiltonian Parameters of the Copper(II) Complexes

		experimental		calculated	
	S	g_1, g_2, g_3	A_1, A_2, A_3 (mT)[a]	g_1, g_2, g_3	A_1, A_2, A_3 (mT)[a]
1	${}^1/_2$	2.042, 2.042, 2.197	3.8, 3.8, 20.3[b]	2.0420, 2.0435, 2.1475	3.8, 3.8, 25.2
$\mathbf{1}H^+$	${}^1/_2$	2.045, 2.045, 2.200	3.6, 3.6, 20.2[b]	2.0415, 2.0446, 2.1486	3.3, 3.8, 24.8
$\mathbf{1}^{2+}$	${}^1/_2$	2.042, 2.042, 2.205	2.5, 2.5, 19.7[b]	2.0428, 2.0439, 2.1447	2.8, 2.9, 24.9
$\mathbf{2}^{2-}$	${}^1/_2$	2.038, 2.038, 2.180	2.0, 2.0, 21.0[b]	2.0435, 2.0440, 2.1414	4.2, 4.2, 24.7

[a]Absolute value. [b]Superhyperfine coupling constants were measured on the triple-derivative spectra: $A_{2H,3}$ = 0.73 and $A_{2N,3}$ = 1.54 for **1** and $\mathbf{1}H^+$; $A_{2H,3}$ = 0.56 and $A_{2N,3}$ = 1.54 mT for $\mathbf{1}^{2+}$; $A_{4N,1} = A_{4N,2}$ = 1.6 mT and $A_{4N,3}$ = 1.3 mT for $\mathbf{2}^{2-}$.

regions of the spectrum (A_{4N} = 1.6 mT in the perpendicular region and A_{4N} = 1.3 mT in the parallel region), as is customary with copper amidato complexes. The g_3 value (2.180) is

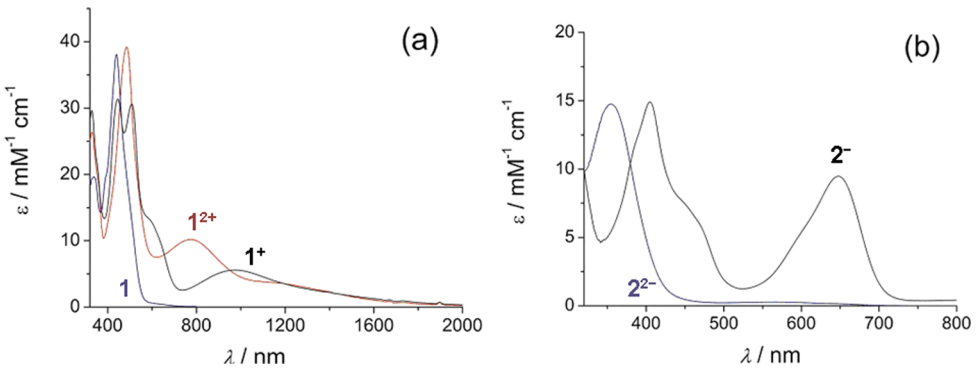

Figure 3. UV−vis−NIR spectra of CH_2Cl_2 solutions: (a) **1** (blue), $\mathbf{1}^+$ (black), and $\mathbf{1}^{2+}$ (red) generated by electrolysis at 233 K. T = 298 K. (b) $\mathbf{2}^{2-}$ (blue) and $\mathbf{2}^-$ (black) generated by electrolysis at 233 K. T = 233 K.

DOI: 10.1021/acs.inorgchem.5b01285
Inorg. Chem. 2015, 54, 9013−9026

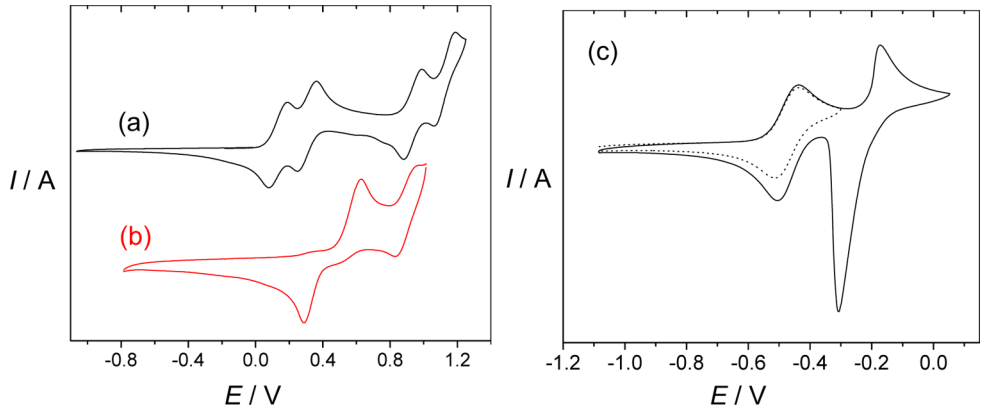

Figure 5. Cyclic voltammograms of 1.0 mM CH_2Cl_2 solutions (+0.1 M nBu_4NClO_4) of (a) **1**, (b) $\mathbf{1H}^+$, and (c) $\mathbf{2}^{2-}$. Potentials are referenced to the Fc^+/Fc redox couple. Scan rate = 100 mV s^{-1} and T = 298 K.

consistent with a square-planar tetraanionic donor set forming a 5.5.5 chelate ring.[18] The EPR parameters were calculated by DFT methods for the parent complexes **1** and $\mathbf{2}^{2-}$, as well as the protonated $\mathbf{1H}^+$ (Table 3). The computed **g** and **A** tensors for all three species are in agreement with the experimental results.

3.4. Electrochemistry of 1 and $\mathbf{2}^{2-}$. The CV of **1** in CH_2Cl_2 (+0.1 M nBu_4NClO_4) displays three quasi-reversible one-electron-oxidation waves at 0.09 V (ΔE_p = 60 mV), 0.22 V (ΔE_p = 60 mV), and 0.82 V (ΔE_p = 80 mV) and an irreversible one at 0.96 V versus Fc^+/Fc (Figure 5a). The first two oxidation potentials match fairly well those measured for the nickel(II) analogue of **1**, namely, $\mathbf{NiL^1}$ (Table 1).[16] Thus, the first two oxidation waves of **1** are assigned to redox processes centered on the tetraaminobenzene ring, yielding successively the π-cation radical and the α-diiminoquinone dication. The highest oxidation waves may correspond to successive oxidations of the phenolate moieties into phenoxyl radicals.[7] However, because of the high potential values, it was not possible to make unambiguous conclusions regarding these two waves. Interestingly, by replacement of nBu_4NClO_4 with nBu_4NPF_6 as the supporting electrolyte, the first two waves are better separated, while the fourth one appears more reversible.[64]

Upon the addition of 1 mol equiv of $HClO_4$, the redox waves of **1** disappeared in the CV in favor of a new redox process characteristic of $\mathbf{1H}^+$, with an oxidation wave at 0.62 V apparently coupled to a cathodic wave at 0.28 V (Figure 5b). The large ΔE_p (340 mV) is evidence that the electron transfer is coupled to a chemical reaction, which, by analogy to $(\mathbf{NiL^1H})^+$ (Table 1), is ascribed to a fast deprotonation, affording $\mathbf{1}^{2+}$.[16] This hypothesis is corroborated by the similarity between $E^{p}_{c}{}^{1}$ of $\mathbf{1H}^+$ and $E^{p}_{c}{}^{2}$ of **1**, as well as the analogy between $E_{1/2}{}^{2}$ of $\mathbf{1H}^+$ and $E_{1/2}{}^{3}$ of **1**. Notably, the first oxidation wave is anodically shifted by more than 300 mV in the presence of protons, consistent with the fact that the protonation site is a basic dimethylamino group.

The CV of $\mathbf{2}^{2-}$ displays a reversible redox wave at $E_{1/2}{}^{1}$ = −0.42 V (ΔE_p = 80 mV) followed by an irreversible anodic signal at $E_p{}^{a,2}$ = −0.10 V (Figure 5c). The latter is associated with a cathodic signal at −0.26 V, whose profile and high intensity may suggest the reduction of neutral **2** adsorbed on the electrode. Changing the supporting electrolyte nBu_4NClO_4 with nBu_4NPF_6 did not improve the solubility of the dication, as judged by the similarity in the shape of the CV curves in these two media. Thus, while the monooxidized species $\mathbf{2}^-$ could be generated in solution, we were unable to prepare the dioxidized complex. It is worth noting that the $I_p{}^{a}/I_p{}^{c,1}$ ratio (corresponding to $E_{1/2}{}^{1}$) is 1.59 for $\mathbf{2}^{2-}$, while it is 1.11 for **1**. This suggests a lower chemical stability of the one-electron-oxidized species in the former case. As expected, the first two oxidations of $\mathbf{2}^{2-}$ occur at much lower potential than those for **1** as a result of the greater donor ability of the deprotonated amidato N atoms compared with that of the neutral imine ones. Conversely, the $E_{1/2}{}^{1}$ potential of $\mathbf{2}^{2-}$ is fairly above the oxidation potential of the copper(II) complex of the tetradeprotonated 1,2-bis(2-hydroxy-2-methylpropanamido)-benzene and some of its derivatives (in the range of −0.835 to −1.080 V).[65] This difference is consistent with the enhanced σ-donating ability of the alkoxo group with respect to the oxamato one, which additionally shifts the oxidation site from the ligand to the metal (Cu^{III}/Cu^{II} redox couple).[65] Further, for several copper complexes formed with tetraanionic ligands *N,N′-o*-phenylenebis(oxamate), a linear relationship was observed between the oxidation potential (Cu^{III}/Cu^{II} redox couple in this series) and the visible absorption maxima corresponding to the d−d band.[18,66] This correlation cannot be extrapolated to complex $\mathbf{2}^{2-}$, supporting a different oxidation site, i.e., the aromatic bridge, in this case.

3.5. Electronic Spectra of the Oxidized Species. The oxidized species $\mathbf{1}^+$ and $\mathbf{1}^{2+}$ were generated by bulk electrolysis at 233 K for spectroscopic characterization. The electrolysis was monitored by RDE voltammetry, yielding >95% of oxidized product. Chemical oxidations gave identical spectroscopic data. In contrast to **1**, the electronic spectra of $\mathbf{1}^+$ and $\mathbf{1}^{2+}$ display absorption bands above 450 nm (Figure 3 and Table 2) that may correspond to copper(II) radical/diiminoquinone species or alternatively to copper(III)/copper(III) radical complexes. The spectrum of $\mathbf{1}^+$ displays transitions at 446, 508, and 972 nm. It is closely related to that of the nickel analogue of $\mathbf{1}^+$, $(\mathbf{NiL^1})^+$,[16] supporting the description of $\mathbf{1}^+$ as a copper(II) π-radical complex. This assignment is further supported by the strong intensity of the visible bands, which stem from intraligand charge-transfer (ILCT) involving the bridging radical moiety (see section 3.7). The derivative of $\mathbf{1}^+$, which does not feature dimethylamino substituents on the central ring, displays a band at 962 nm (ε = 1500 M^{-1} cm^{-1}) as well as a NIR band at 1890 nm (ε = 2900 M^{-1} cm^{-1}).[53c] Similar features were reported for another derivative that harbors methoxy substituents on the aromatic bridge: 1075 nm (ε =

DOI: 10.1021/acs.inorgchem.5b01285
Inorg. Chem. 2015, 54, 9013−9026

6400 M^{-1} cm^{-1}) and 1653 nm (ε = 6300 M^{-1} cm^{-1}).[53b] In these two complexes, the ligand-radical singly occupied MO (SOMO) is either centered on the peripheral rings (phenoxyl radical) or shared between the three rings (delocalized radical).[53b,c] The absence of an NIR band in the region 1600−1900 nm in the case of $\mathbf{1}^+$ suggests that the ligand-radical SOMO does not extend onto the phenolate donors. The visible−NIR spectrum of $\mathbf{1}^{2+}$ displays transitions at 330, 486, and 778 nm. The absence of an NIR band rules out the fact that $\mathbf{1}^{2+}$ consists of both a bridging π radical and phenoxyl radicals. The visible bands are consistently assigned by TD-DFT to both ILCT and metal-to-ligand charge-transfer (MLCT) involving the α-diiminoquinone moiety and the Cu ion.

The spectrum of $\mathbf{2}^-$ shows intense transitions at 648 and 405 nm with a shoulder at ca. 450 nm (Figure 3). Although red-shifted, it resembles the spectrum of the nickel(II) (π-radical) species $[NiL^2]^-$.[17] A copper(III) oxamato complex has been previously reported with the unsubstituted analogue of $\mathbf{2}^-$.[54] Its visible spectrum showed transitions of up to 580 nm, but their intensity was much smaller. This argues against the assignment of $\mathbf{2}^-$ as a copper(III) complex and reinforces the idea that it has copper(II) π-radical character.

3.6. EPR Spectra of the Oxidized Species. The 10 K EPR spectrum of the electrochemically generated $\mathbf{1}^+$ in CH_2Cl_2 (+0.1 M nBu_4NPF_6)[67] is depicted in Figure 6. It exhibits a broad dominant signal at $g \approx 2$ that is assigned to $\mathbf{1}^+$, which superimposes to an $S = {}^1/_2$ signal corresponding to **1** present as an impurity in the sample. The presence of a half-field signal (g = 4.3) is evidence for a triplet S = 1 spin state of $\mathbf{1}^+$, which can only result from magnetic coupling between copper(II) and radical spins. This assumption is confirmed by the observation of a four-line pattern in this transition, arising from the hfc of the electronic spins with one copper nuclear spin.[68] Thus, the present data unequivocally rule out the formulation of $\mathbf{1}^+$ as a copper(III) complex, which would be diamagnetic. The triplet signal at $g \approx 2$ is large, similar to the situation found for weakly exchange-coupled nitroxide copper(II) triads.[69] It could be simulated by using the ZFS parameters $|D| = 0.030 \pm 0.004$ cm^{-1}, E/D = 0.27, and an isotropic g value of 2.02.

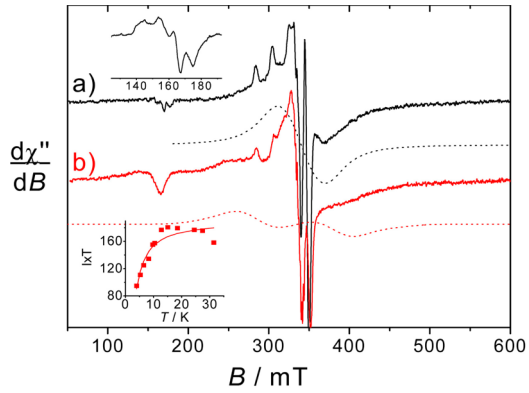

Figure 6. X-band EPR spectrum of a 1 mM CH_2Cl_2 solution of the electrochemically generated one-electron-oxidized species: (a) $\mathbf{1}^+$; (b) $\mathbf{2}^-$ after three cycles of freezing/thawing. Microwave frequency = 9.68 GHz, power = 10 mW (a) or 20 mW (b), modulation frequency = 100 kHz, amperage = 0.4 mT, and T = 8 K. Solid black lines: Experimental spectra. Red dotted lines: Simulations using the parameters given in the text. Top inset: Zoom of the ΔM_S = 2 region for $\mathbf{1}^+$ (52 scans). Bottom inset: Fit of the $I \times T$ as a function of T according to a Bleaney−Bowers model for the half-field resonance of $\mathbf{2}^-$.

Interestingly, the ZFS parameters reported for copper(II) phenoxyl radical salen complexes are usually close to or larger than the X-band quantum (0.35 cm^{-1}) because of the short interspin distance.[14,15,53] In $\mathbf{1}^+$, one unpaired electron is mainly hosted by the dimethylamino substituents and neighboring C atoms, and thus far from the metal center. The ZFS parameters are consequently much smaller, making the triplet detectable at the X-band frequency. This behavior resembles that reported for copper phenoxyl complexes formed with tripodal ligands based on the bis(2-pyridylmethyl)amine[68,70] and some copper(II) nitroxide complexes where the radical is axially bound.[69,71] Interestingly, the qualitative point−dipole approximation leads to a SS separation of ca. 4.1 Å, which is smaller than the Cu···$N_{dimethylamino}$ distance (6.5 Å). This attests that the unpaired electrons are somewhat delocalized over the bridging unit (π radical). Also noticeable is the difference of ZFS parameters between $\mathbf{1}^+$ and its dimethoxy derivative.[53b] Because of the weaker electron-donating ability of MeO substituents, the central-ring orbitals involved in the ZFS are developed closer to the metal, thus inducing a higher $|D|$ value.

The 10 K EPR spectrum of the electrogenerated $\mathbf{1}^{2+}$ contrasts sharply with that of $\mathbf{1}^+$. It displays an axial $S = {}^1/_2$ signal with hyperfine splitting due to the interaction of the electronic spin with the copper nuclear spin (Figure 3c and Table 3). The g and A parameters obtained from simulation are typical for an $S = {}^1/_2$ mononuclear copper(II) complex, consistent with the unpaired electron residing in a copper rather than a ligand orbital. Thus, the ligand bridge has been doubly oxidized (α-diiminoquinone ring), and $\mathbf{1}^{2+}$ is described as a closed-shell dioxidized salophen ligand coordinated to a Cu^{II} ion. It is worth noting that the g_3 value order is **1** (2.197) < $\mathbf{1}H^+$ (2.200) < $\mathbf{1}^{2+}$ (2.205), consistent with the ligand-field strength in the order $\mathbf{1}^{2+}$ < $\mathbf{1}H^+$ < **1**. This trend matches the increase in positive charge at the bridging ring upon going from **1** to $\mathbf{1}^{2+}$. The high g_3/A_3 value is also consistent with slightly increased distortion in the copper(II) geometry in $\mathbf{1}^{2+}$.[62,63] Staab et al. described the X-ray crystal structure of doubly oxidized 1,2,4,5-tetrakis(dimethylamino)benzene.[57] They observed 1,3-diaminoallyl distributions of bond lengths in the two N−C−C−C−N fragments, which are consequently planar. The fragments are strongly tilted one against the other, inducing a twisted conformation of the benzene ring as a result of a diminished aromaticity. Such a conformation may explain the increased distortion in $\mathbf{1}^{2+}$ in comparison with that in **1** (Figure S23).

Electrochemical oxidation of $\mathbf{2}^{2-}$ is initially accompanied by a quenching of the copper(II) EPR signal (Figure S16). Spin quantification reveals that the residual copper(II) signal accounts for 5−10% of the original one, in agreement with the Faraday yield of the electrolysis (0.95 electron removed) and RDE coulometry. After three freeze/thaw cycles, however, a characteristic triplet signal appears for the one-electron-oxidized species (Figure 6b). This signal is close to, but not superimposable on, that of $\mathbf{1}^+$. In particular, the ΔM_S = 1 transitions are more separated in $\mathbf{2}^-$, indicative of a larger D value. The change in magnetism of $\mathbf{2}^-$ (from diamagnetic, or weakly paramagnetic, to paramagnetic) resulting from modification of the solvent properties resembles the behavior reported in the early 1970s for Würster's blue cation. This radical salt has been shown to be either paramagnetic or almost diamagnetic, depending on the phase, pressure, and temperature.[72] Several hypotheses were proposed to explain this behavior, with the most plausible being the formation of

DOI: 10.1021/acs.inorgchem.5b01285
Inorg. Chem. 2015, 54, 9013−9026

diamagnetic ion pairs under certain conditions. Whether CT (i.e., disproportionation of the radical) occurs in the dimer remained a matter of debate for a long time in the literature.[72] Similarly, dimers were proposed to account for the diamagnetism of a priori paramagnetic nickel complexes involving coordinated α-diiminosemiquinonate radicals.[10] The existence of monomer−dimer equilibrium may account for a change in the paramagnetism of $\mathbf{2}^-$ after several freeze/thaw cycles. It is not observed for $\mathbf{1}^+$, likely because of the steric demands of the *tert*-butyl groups that prevent dimerization.

In order to accurately determine the ZFS parameters of $\mathbf{2}^-$ and ensure that no species having a ZFS larger than 0.35 cm^{-1} (X-band energy quantum) was present,[73] we conducted a multifrequency EPR study (9.6, 220, and 330 GHz; Figures 7 and S30) on a solid sample of $\mathbf{2}^-$.[74] The radical complex $[PPh_4]\mathbf{2}$ was isolated as a highly hygroscopic and thermally unstable dark-green solid after chemical oxidation with ferrocenium hexafluorophosphate in CH_2Cl_2 at 213 K, followed by argon flushing. The triplet spectrum of a frozen CH_2Cl_2 solution of $[PPh_4]\mathbf{2}$ was identical with that of the electrochemically generated $\mathbf{2}^-$ at 9.63 GHz. The 220 GHz spectrum of solid $[PPh_4]\mathbf{2}$ consists of two superimposed signals. One signal comprises two resonances at $g_{\|}$ = 2.181 (ca. 7.25 T) and $g_{\perp}$ = 2.035 (ca. 7.75 T), which match the values obtained for $\mathbf{2}^{2-}$ at X-band frequency. Further support for the assignment of these signals to an $S = {}^1/_2$ system comes from the shift in the resonance field observed upon increasing the frequency to 330 GHz. Thus, the resonances at 7.25 and 7.75 T can be safely attributed to $\mathbf{2}^{2-}$ present as an impurity in the sample. Most importantly, two satellite resonances are observed at 7.68 and 7.80 T (at 220 GHz) or 11.54 and 11.66 T (at 330 GHz). The fact that the resonance separation is independent of the frequency in this case indicates that the signals arise from a triplet system, with the ZFS dominating the energy separation. From simulation of the spectra recorded at the three frequencies, the ZFS parameters could be estimated as D = 0.11 ± 0.01 cm^{-1} and E/D = 0, with an isotropic g value of 2.039. It has to be emphasized that the triplet resonances remain barely resolved in the high-field spectra because of significant overlap with the signal of $\mathbf{2}^{2-}$, which cannot be avoided in the preparation. Consequently, the confidence level on the ZFS parameters remains large, even with a multifrequency EPR study. It is remarkable that the $|D|$ value obtained for $\mathbf{2}^-$ is about 4 times larger than that measured for $\mathbf{1}^+$. The interaction between the two unpaired electrons is therefore stronger in $\mathbf{2}^-$, mostly because of the increased covalency of the copper−amidato bonds, which harbor some of the spin density (see section 3.7).

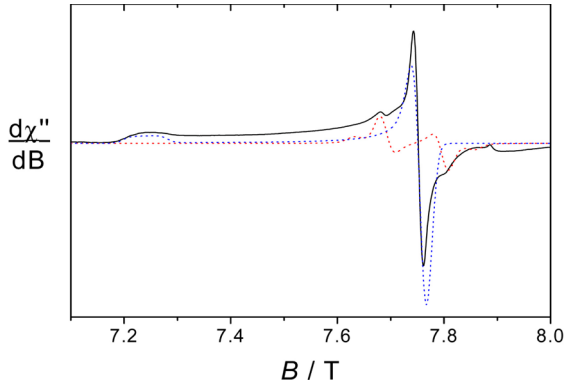

Figure 7. Powder EPR spectra of $[PPh_4]\mathbf{2}$ at 220 GHz. T = 10 K. Solid lines: Experimental spectra. Dotted lines: Simulations for a mononuclear $S = {}^1/_2$ species (blue, $g_{\|}$ = 2.181, $A_{\|}$ = 21 mT for a copper nucleus, $g_{\perp}$ = 2.035) and a triplet species (red, D = 0.11 cm^{-1}, E/D = 0, g = 2.039).

In order to gain insight into the nature of the magnetic coupling between the radical and copper(II) spins, we investigated the temperature dependence of the EPR spectrum. The plot of $I \times T$ as a function of $1/T$ (where I is the doubly integrated half-field signal) slightly deviates from linearity for $\mathbf{2}^-$, indicating that the coupling is weakly antiferromagnetic.[75] Regarding $\mathbf{1}^+$, the changes are within the experimental error and cannot be analyzed accurately. The data of $\mathbf{2}^-$ could be satisfactorily fitted by using a Bleaney−Bowers model,[76] indicating that the dimer and monomer are not in thermal equilibrium in the investigated temperature range. The triplet−singlet gap Δ is calculated at 4.8 ± 0.3 cm^{-1}. This value is much larger than the ZFS parameters, confirming that treatment of the spectrum by considering an isolated triplet spin is correct. It is consistent with weak coupling due to the spatial separation of the two spins and within the range of those reported for copper(II) nitroxide triads.[69]

3.7. DFT Calculations. *Energetic and Structural Analysis.* Energetic analysis was performed to confirm the radical state of $\mathbf{1}^+$ and $\mathbf{2}^-$ and rule out a singlet copper(III) state. By looking at the highest occupied MO (HOMO)−SOMO energy separation in parent complexes **1** and $\mathbf{2}^{2-}$, one can gain insight into the oxidation locus. The SOMOs of parent complexes **1** and $\mathbf{2}^{2-}$, mainly of $3d(x^2-y^2)$ character, are only 1.5 and 4.9 kcal mol^{-1} above their respective HOMOs, of ligand character. These rather small values highlight the close proximity of metal- and ligand-based orbitals. In this case, the oxidation is likely to occur from the HOMO because it alleviates the energy cost associated with having an electron pair. Accordingly, the calculated free energies of the copper(III) and copper(II) radical forms of the complexes in CH_2Cl_2 predict the copper(II) radical species to be lower in energy by 21.7 and 20.0 kcal mol^{-1} for $\mathbf{1}^+$ and $\mathbf{2}^-$, respectively. For the doubly oxidized species $\mathbf{1}^{2+}$, we considered two putative formulations, quartet copper(II) diradical or doublet copper(II) states. The calculated free energies predict the doublet copper(II) species to be more stable by 6.0 kcal mol^{-1}, showing that the second oxidation process is again ligand-centered to provide a closed-shell ligand.

The computed structural rearrangements upon going from **1** to $\mathbf{1}^+$ and to $\mathbf{1}^{2+}$ are consistent with oxidations occurring on the central ring. Indeed, the C−C and C−O bond lengths within the phenolic rings of **1**, $\mathbf{1}^+$, and $\mathbf{1}^{2+}$ are similar within ±0.01 Å, while the N−Cu and O−Cu bond lengths do not vary by more than 0.003 Å (Figures S17−S20). In contrast, drastic variations in the bond distances are observed within the tetraaminobenzene ring upon oxidation: a vinylogous distribution of bond lengths appears in $\mathbf{1}^+$, which is exacerbated in $\mathbf{1}^{2+}$. The same analysis applies upon examination of the structural rearrangements induced by oxidation of $\mathbf{2}^{2-}$ into $\mathbf{2}^-$, which mainly concern the central benzene ring (Figures S21 and S22). The magnitude of the variation differs somewhat between $\mathbf{1}^+$ and $\mathbf{2}^-$ because of the difference in the connecting group between the central benzene ring and O-atom donors. In addition to bond-length variations, the bis(dimethylamino) central ring undergoes significant torsions upon oxidation (Figure S23). This reflects the increasing need for electron donation from the

DOI: 10.1021/acs.inorgchem.5b01285
Inorg. Chem. 2015, 54, 9013−9026

substituents inasmuch as the ring loses its aromaticity and becomes electron-poor. The spin-density plots of the monooxidized triplets $\mathbf{1}^{+}$ and $\mathbf{2}^{-}$ are shown in Figure 8. The

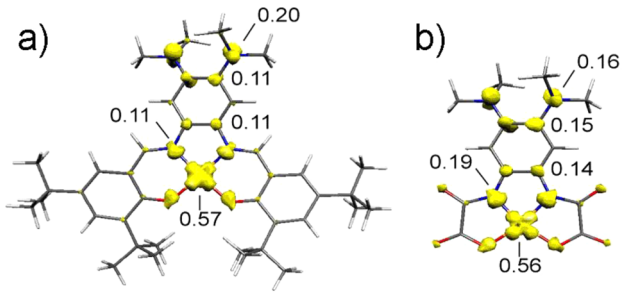

Figure 8. Spin-density plots, including the values of the most important individual spin populations, for (a) triplet $\mathbf{1}^{+}$ and (b) triplet $\mathbf{2}^{-}$.

Mulliken spin density is spread over the central part of the complexes, with positive spin populations found mainly at the Cu ion (0.57 for $\mathbf{1}^{+}$ and 0.56 for $\mathbf{2}^{-}$) and the bridging unit. Importantly, the coordinated N atoms hold more spin density in $\mathbf{2}^{-}$ than in $\mathbf{1}^{+}$, while the dimethylamino groups hold less. This is in line with the greater participation of the better π-donor $N_{amidato}$ (formally negative) in the resonance structure of the radical, compared with the neutral N_{imine} donor. Regarding the SOMOs (Figures S24 and S25), the first one is metal-based with a Cu 3d(x^2-y^2) contribution similar to that of the SOMOs in the parent complexes **1** and $\mathbf{2}^{2-}$. The second SOMO is ligand-based with a composition similar to that of the SOMOs in the oxidized proligands $(H_2\mathbf{L}^{1})^{+}$ and $(Et_2H_2\mathbf{L}^{2})^{+}$, without any contribution from the metal ion.

Computed Spectroscopic Properties. Because oxidized species $\mathbf{1}^{+}$ and $\mathbf{2}^{-}$ are magnetically coupled systems with a total ground spin state of $S > {}^{1}/_{2}$, we carried out CASSCF-based ab initio calculations in an attempt to model the ZFS parameters of both complexes. The following values were obtained: D = +0.024 cm^{-1} (E/D = 0.267) for $\mathbf{1}^{+}$ and D = +0.839 cm^{-1} (E/D = 0.136) for $\mathbf{2}^{-}$. In these complexes, the ZFS is caused by the combined effect of the magnetic dipole–dipole interaction and the exchange-coupling anisotropy. The first one is the SS contribution, which is a first-order term involving direct dipolar SS interactions between pairs of electrons. This contribution is expected to be dominant in organic triplets or radicals and calculated at D^{SS} = 0.027 and 0.021 cm^{-1} for $\mathbf{1}^{+}$ and $\mathbf{2}^{-}$, respectively. The exchange contribution is a relativistic term that originates from the coupling of the excited state(s) and the ground state of the magnetic centers by spin–orbit interaction. The magnitude of this contribution was found to be negligible for $\mathbf{1}^{+}$ and dominant for $\mathbf{2}^{-}$, with D^{SOC} = 0.003 and 0.848 cm^{-1}, respectively. Although the ZFS parameters are largely overestimated in $\mathbf{2}^{-}$, the order of the computed ZFS parameters $\mathbf{1}^{+}$ < $\mathbf{2}^{-}$ reproduces the experimental trend. As mentioned above, the π-ligand-radical SOMO extends to the peripheral amidates in $\mathbf{2}^{-}$. The interaction of the ligand radical with the metal-based SOMO is therefore stronger, explaining these larger ZFS parameters.

TD-DFT calculations were undertaken on the optimized structures of the doublet states of **1**, $\mathbf{2}^{2-}$, and $\mathbf{1}^{2+}$ and the triplet states of $\mathbf{1}^{+}$ and $\mathbf{2}^{-}$ (Figures 9 and S26–S28). TD-DFT calculations systematically result in a good match between the

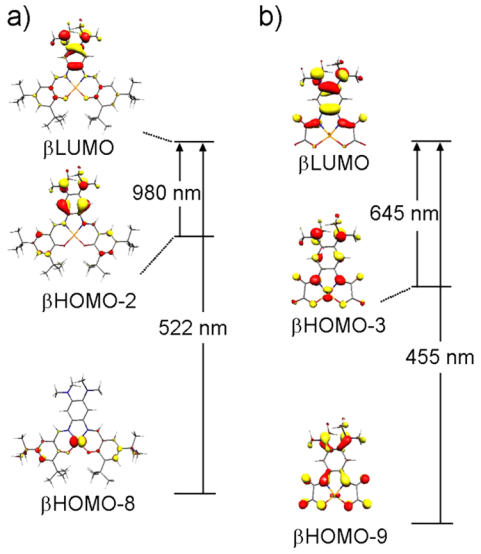

Figure 9. TD-DFT assignment of the vis–NIR bands for (a) triplet $\mathbf{1}^{+}$ and (b) triplet $\mathbf{2}^{-}$.

predicted and experimental absorption bands. Only the results obtained for the radical complexes are discussed in this section. For $\mathbf{1}^{+}$, the lowest-energy electronic excitation corresponds to a β-HOMO−2 → β-LUMO transition. It is predicted at 980 nm (f = 0.132) and arises from an ILCT, with both the donor and acceptor orbitals being ligand-based MOs centered on the bridging radical unit. The second lowest-energy transition (522 nm, f = 0.606) is a MLCT, wherein the acceptor orbital is distributed over the central ring (β-HOMO−8 → β-LUMO). Regarding $\mathbf{2}^{-}$, the first electronic excitation of significant oscillator strength is calculated at 645 nm (f = 0.207). Its origin differs from the lowest-energy band calculated for $\mathbf{1}^{+}$ by the contribution of the oxamato groups (Figure 9). It mainly arises from ILCT/ligand-to-ligand charge-transfer (LLCT), wherein both the donor and acceptor orbitals are distributed over the oxamato and bridging radical units (β-HOMO−3 → β-LUMO). The second calculated excitation (455 nm, f = 0.258) is similar in origin (ILCT/LLCT), although it arises from a β-HOMO−9 → β-LUMO transition. Overall, the agreement between the experimental and calculated spectra confirms not only the radical nature of the species but also that the central ring is the prime locus of oxidation in these complexes.

3.8. Aerobic Oxidation of Benzyl Alcohol. The catalytic performances of **1** and $\mathbf{2}^{2-}$ were evaluated for the aerobic oxidation of benzyl alcohol. In a typical experiment, the catalyst loading was 1 mM in the presence of 20 equiv of potassium *tert*-butoxide (tBuOK). Production of benzaldehyde was monitored by gas chromatography. When benzyl alcohol is used as the solvent (under a 1 bar atmosphere of dioxygen), we observed a linear increase of the benzaldehyde concentration as a function of time during the first 24 h for $\mathbf{2}^{2-}$, followed by a decrease in the yield for a longer period (Figure 10). The turnover number (TON) reaches 10 at 24 h, corresponding to a turnover frequency (TOF) of 0.42 h^{-1}. Complex **1** was found to be much less efficient, with only 0.7 turnover achieved after 20 h (TOF = 0.035 h^{-1}) and 1.1 turnover after 47 h.

Stack et al. reported that catalytic oxidation of benzyl alcohol in a basic medium by salen-type copper(II) bis(phenolate) complexes proceeds in a two-step mechanism.[77] First the precatalyst is slowly oxidized into its active radical form by

DOI: 10.1021/acs.inorgchem.5b01285
Inorg. Chem. 2015, 54, 9013–9026

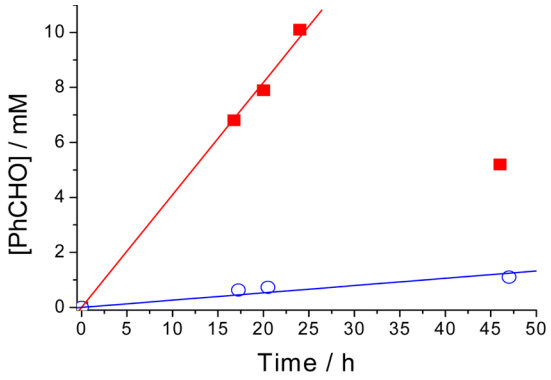

Figure 10. Aerobic oxidation of benzyl alcohol by **1** (blue circles) and $\mathbf{2}^{2-}$ (red squares). The conditions are indicated in the text.

dioxygen. This phenomenon is accompanied by a lag time during the first hours of catalysis. Once the radical is formed, catalysis proceeds linearly to finally reach a plateau. In the case of $\mathbf{2}^{2-}$, the aldehyde concentration grows linearly with time. The absence of lag time indicates that oxidation by dioxygen occurs faster with $\mathbf{2}^{2-}$, consistent with its lower oxidation potential with respect to both **1** and Stack et al.'s complexes.

The catalytic performance of the complexes was affected by the solvent. Using a 2 M CH_2Cl_2 solution of benzyl alcohol, a TON of 3 was measured for **1** after 4 days (Figure S31), while it is 9 after 24 h and remains stable for 2 days in the case of $\mathbf{2}^{2-}$. When a 0.1 M CH_2Cl_2 solution of benzyl alcohol was used, the TON did not exceed 1 for $\mathbf{2}^{2-}$ after 72 h, while it again reached 3 for **1** after 72 h, by using a higher dioxygen pressure (2 bar). With $\mathbf{2}^{2-}$, the benzaldehyde yield is lower in the 0.1 M benzyl alcohol medium than when pure benzyl alcohol is the solvent. This behavior can be understood in terms of the solubility of $\mathbf{2}^{2-}$. The solution of $\mathbf{2}^{2-}$ indeed became colored in neat benzyl alcohol (containing 0.02 M tBuOK), attesting to its solubility. In CH_2Cl_2 that contains the same amount of tBuOK, $[PPh_4]_2\mathbf{2}$ remains insoluble and the solution is colorless. Thus, the catalytic efficiency directly correlates with the solubility of the precatalyst in the CH_2Cl_2 medium, whereas it is mainly affected by the oxidation potential of the complexes in neat benzyl alcohol. At a 2 M substrate concentration, i.e., where both **1** and $\mathbf{2}^{2-}$ are substantially reactive, we conducted experiments with α-benzyl-d_2 alcohol ($PhCD_2OD$). We did not detect a large kinetic isotope effect (KIE) for **1** (Figure S31), as reported for benzyl alcohol oxidation by copper(II) radical salophen complexes substituted by electron-donating groups.[53c] This behavior was interpreted by the fact that the rate-determining step in the oxidation reaction does not involve hydrogen abstraction from the α position of the benzyl alcohol.[53c] Regarding $\mathbf{2}^{2-}$, benzaldehyde production did not occur during the first 1 h, but a rapid increase in the product concentration was observed after this activation period whether $PhCH_2OH$ and $PhCD_2OD$ are used, again suggesting that the KIE is within the uncertainty of the experiment. In order to gain insight into the nature of the intermediates that form during oxidation, most particularly in the case of $\mathbf{2}^{2-}$, we realized spin-trapping experiments by using the radical scavenger phenyl-*N*-*tert*-butyl nitrone (PBN). The choice of this spin trap was motivated by the recent identification of several PBN-radical adducts formed in the course of benzaldehyde and benzyl alcohol oxidations.[78] The EPR spectrum of PBN (0.1 M) in a benzyl alcohol/CH_2Cl_2 (1:1) mixture consists of a very weak signal centered at g_{iso} = 2.006 (in both the absence and presence of 0.02 M tBuOK), consistent with the Hutchings works.[78] When **1** (0.6 mM) was added to PBN (0.1 M) in a benzyl alcohol/CH_2Cl_2 (1:1) solution in the presence of 0.02 M tBuOK, we observed the dominant copper lines superimposed on the same weak signal as in the absence of the complex (Figure S32). Replacing **1** by $\mathbf{2}^{2-}$ results in a dramatic increase in the intensity of the EPR signal centered at g_{iso} = 2.006, attesting that a larger amount of radical is trapped by PBN. The identity of the radical was obtained by simulation of the spectrum (Figures S33 and S34), which gives the following spin-Hamiltonian parameters: A_N = 1.44 mT and A_H = 0.26 mT. These values nicely fit with those reported for the PBN adduct of the α-hydroxybenzyl radical $[PhCHOH]^{\bullet}$ (A_N = 1.49−1.51 mT and A_H = 0.23−0.26 mT).[78] The slightly lower A_N value herein obtained likely results from the lower polarity of the benzyl alcohol/CH_2Cl_2 (1:1) mixture (neat benzyl alcohol or benzyl alcohol benzaldehyde mixtures were used in the Hutchings work).[71] These results show that aerobic benzyl alcohol oxidation by $\mathbf{2}^{2-}$ proceeds through abstraction of the C_α−H bond H atom, presumably by the radical complex $\mathbf{2}^{-}$ formed by air oxidation, producing a transient α-hydroxybenzyl radical $[PhCHOH]^{\bullet}$. As shown above, $\mathbf{2}^{2-}$ is more reactive toward benzyl alcohol oxidation than **1** at high substrate concentration. The higher intensity of the EPR signal of the PBN radical adduct in the case of $\mathbf{2}^{2-}$ is consistent with a higher concentration of the α-hydroxybenzyl radical, which nicely correlates with the above catalytic results.

4. CONCLUSIONS

In summary, bis(dimethylamino) substitution on the central ring of the copper(II) salophen and copper(II) bis(oxamato) platforms confers redox noninnocence upon the aromatic bridge. The first oxidation process occurs at lower potentials ($E^1_{1/2}$ value in the range of −0.45 to +0.09 V vs Fc^+/Fc) in comparison to those of copper salen complexes, a key feature to impart "noble" metal character to first-row transition metals.[1e] The lower redox potential for $\mathbf{2}^{2-}$ than for **1** is mainly due to the stronger π-donating ability of the amidates. It is significant that the unsubstituted derivative of $\mathbf{2}^{2-}$, namely, $[Cu^{II}opba]^{2-}$ (Scheme 2c), exhibits a metal-centered oxidation, with an irreversible Cu^{III}/Cu^{II} redox wave. The present results show that two NMe_2 substituents on the aromatic ring make the oxidized product much more accessible (from a thermodynamic point of view) and stable. Further, they induce a shift in the oxidation site from the metal to the ligand. It is remarkable that the decrease in the oxidation potential with respect to the unsubstituted compounds is very similar (ca. 0.5 V) in both the salophen and oxamato families. It may therefore be extrapolated to other ligand platforms. In the one-electron-oxidized species ($\mathbf{1}^{+}$ and $\mathbf{2}^{-}$), the radical spin is mainly hosted by the central bis(dimethylamino)-substituted ring (π radical). It is magnetically coupled to the copper(II) spin, affording S = 1 systems that can be characterized by X-band EPR spectroscopy. The greater donating ability of the amido fragments, which hosts part of the spin density induces a higher $|D|$ value for $\mathbf{2}^{-}$. Finally, we show that both **1** and $\mathbf{2}^{2-}$ catalyze the aerobic oxidation of benzyl alcohol under basic conditions. Complex $\mathbf{2}^{2-}$ is more efficient at high benzyl alcohol concentration because of its lower oxidation potential, which makes the radical easier to form by air oxidation.

DOI: 10.1021/acs.inorgchem.5b01285
Inorg. Chem. 2015, 54, 9013−9026

■ ASSOCIATED CONTENT

Supporting Information

The Supporting Information is available free of charge on the ACS Publications website at DOI: 10.1021/acs.inorgchem.5b01285.

Additional electrochemical data, UV−vis titration with $HClO_4$, and DFT data (PDF)

Crystallographic CIF files (CCDC 986938−986941) (CIF)

■ AUTHOR INFORMATION

Corresponding Authors

*E-mail: dr.x@concordia.ca (X.O.).

*E-mail: fabrice.thomas@ujf-grenoble.fr (F.T.).

Present Address

[¶]M.O.: Institut des Sciences Moléculaires de Marseille, Aix Marseille Université, CNRS, Centrale Marseille, ISM2 UMR 7313, Avenue Escadrille Normandie-Niémen, 13397 Marseille Cedex 20, France.

Author Contributions

All authors have given approval to the final version of the manuscript.

Notes

The authors declare no competing financial interest.

■ ACKNOWLEDGMENTS

This work was funded by the CNRS (France), the Labex ARCANE (ANR-11-LABX-0003-01, France), and an NSERC Discovery grant (Canada). X-ray diffraction data were collected on a CFI-funded infrastructure (Canada).

■ REFERENCES

(1) (a) Pierre, J. L. *Chem. Soc. Rev.* **2000**, *29*, 251. (b) Hicks, R. G. *Org. Biomol. Chem.* **2006**, *5*, 1321. (c) Kaim, W.; Schwederski, B. *Coord. Chem. Rev.* **2010**, *254*, 1580. (d) Chirik, P. J.; Wieghardt, K. *Science* **2010**, *327*, 794. (e) Dzik, W. I.; van der Vlugt, J. I.; Reek, J. N. H.; de Bruin, B. *Angew. Chem., Int. Ed.* **2011**, *50*, 3356. (f) Eisenberg, R.; Gray, H. B. *Inorg. Chem.* **2011**, *50*, 9741. (g) Kaim, W. *Inorg. Chem.* **2011**, *50*, 9752. (h) Pierpont, C. G. *Inorg. Chem.* **2011**, *50*, 9766. (i) Scarborough, C. C.; Wieghardt, K. *Inorg. Chem.* **2011**, *50*, 9773. (j) Heyduk, A. F.; Zarkesh, R. A.; Nguyen, A. I. *Inorg. Chem.* **2011**, *50*, 9849. (k) van der Vlugt, J. I. *Eur. J. Inorg. Chem.* **2012**, *2012*, 363. (l) Blanchard, S.; Derat, E.; Desage-El Murr, M.; Fensterbank, L.; Malacria, M.; Mouriès-Mansuy, V. *Eur. J. Inorg. Chem.* **2012**, *2012*, 376. (m) Sieh, D.; Schlimm, M.; Andernach, L.; Angersbach, F.; Nückel, S.; Schöffel, J.; Šušnjar, N.; Burger, P. *Eur. J. Inorg. Chem.* **2012**, *2012*, 444. (n) Caulton, K. G. *Eur. J. Inorg. Chem.* **2012**, *2012*, 435. (o) Luca, R. A.; Crabtree, R. H. *Chem. Soc. Rev.* **2013**, *42*, 1440.

(2) (a) Whittaker, J. W. In *Metal Ions in Biological Systems*; Sigel, H., Sigel, A., Eds.; Marcel Dekker: New York, 1994; Vol. *30*, p 315. (b) Borman, C. D.; Saysell, C. G.; Sokolowski, A.; Twitchett, M. B.; Wright, C.; Sykes, A. G. *Coord. Chem. Rev.* **1999**, *190−192*, 771. (c) McPherson, M. J.; Parsons, M. R.; Spooner, R. K.; Wilmot, C. M. In *Handbook for metalloproteins*; Messerschmidt, A., Huber, R., Poulos, T., Wieghardt, K., Eds.; John Wiley and Sons: New York, 2001; Vol. *2*, p 1272. (d) Whittaker, J. W. In *Advances in Protein Chemistry*; Richards, F. M., Eisenberg, D. S., Kuriyan, J., Eds.; Academic Press, Elsevier: London, 2002; Vol. *60*, p 1. (e) Whittaker, J. W. *Chem. Rev.* **2003**, *103*, 2347. (f) Rogers, M. S.; Dooley, D. M. *Curr. Opin. Chem. Biol.* **2003**, *7*, 189. (g) Firbank, S. J.; Rogers, M.; Hurtado-Guerrero, R.; Dooley, D. M.; Halcrow, M. A.; Phillips, S. E. V.; Knowles, P. F.; McPherson, M. J. *Biochem. Soc. Trans.* **2003**, *31*, 506.

(3) (a) Li, H. In *Handbook for metalloproteins*; Messerschmidt, A., Huber, R., Poulos, T., Wieghardt, K., Eds.; John Wiley and Sons: New York, 2001; Vol. *1*, p 267. (b) Que, L., Jr.; Tolman, W. B. *Nature* **2008**, *455*, 333. (c) Rittle, J.; Green, M. T. *Science* **2010**, *330*, 933. (d) Ortiz de Montellano, P. R. *Chem. Rev.* **2010**, *110*, 932. (e) Browett, W. R.; Stillman, M. J. *Biochim. Biophys. Acta* **1981**, *660*, 1. (f) Ortiz de Montellano, P. R. In *Biocatalysis Based on Heme Peroxidases*; Torres, E., Ayala, M., Eds.; Springer-Verlag: Berlin, 2010; p 79.

(4) (a) Reichard, P. *Trends Biochem. Sci.* **1997**, *22*, 81. (b) Stubbe, J.; van der Donk, W. A. *Chem. Rev.* **1998**, *98*, 705. (c) Fontecave, M. *Cell. Mol. Life Sci.* **1998**, *54*, 684. (d) Stubbe, J.; Nocera, D. G.; Yee, C. S.; Chang, M. C. Y. *Chem. Rev.* **2003**, *103*, 2167.

(5) (a) Chaudhuri, P.; Wieghardt, K. *Prog. Inorg. Chem.* **2002**, *50*, 151. (b) Thomas, F. *Eur. J. Inorg. Chem.* **2007**, *2007*, 2379. (c) Thomas, F. In *Stable Radicals: Fundamentals and Applied Aspects of Odd-Electron Compounds*; Hicks, R. G., Ed.; John Wiley and Sons: Chichester, U.K., 2010; p 281. (d) Kaim, W.; Schwederski, B. *Coord. Chem. Rev.* **2010**, *254*, 1580. (e) Shimazaki, Y.; Yamauchi, O. *Indian J. Chem.* **2011**, 383.

(6) Kadish, K. M.; Caemelbecke, E. V.; Royal, G. In *The Porphyrin Handbook*; Kadish, K. M., Smith, K. M., Guilard, R., Eds.; Academic Press: London, 2000; pp 1−114.

(7) (a) Shimazaki, Y.; Tani, F.; Fukui, K.; Naruta, Y.; Yamauchi, O. *J. Am. Chem. Soc.* **2003**, *125*, 10512. (b) Rotthaus, O.; Jarjayes, O.; Thomas, F.; Philouze, C.; Perez Del Valle, C.; Saint-Aman, E.; Pierre, J. L. *Chem. - Eur. J.* **2006**, *12*, 2293. (c) Rotthaus, O.; Thomas, F.; Jarjayes, O.; Philouze, C.; Saint-Aman, E.; Pierre, J. L. *Chem. - Eur. J.* **2006**, *12*, 6953. (d) Shimazaki, Y.; Yajima, T.; Tani, F.; Karasawa, S.; Fukui, K.; Naruta, Y.; Yamauchi, O. *J. Am. Chem. Soc.* **2007**, *129*, 2559. (e) Storr, T.; Wasinger, E. C.; Pratt, R. C.; Stack, T. D. P. *Angew. Chem., Int. Ed.* **2007**, *46*, 5198. (f) Benisvy, L.; Kannappan, R.; Song, Y. F.; Milikisyants, S.; Huber, M.; Mutikainen, I.; Turpeinen, U.; Gamez, P.; Bernasconi, L.; Baerends, E. J.; Hartl, F.; Reedijk, J. *Eur. J. Inorg. Chem.* **2007**, *2007*, 631. (g) Rotthaus, O.; Labet, V.; Philouze, C.; Jarjayes, O.; Thomas, F. *Eur. J. Inorg. Chem.* **2008**, *2008*, 4215. (h) Rotthaus, O.; Jarjayes, O.; Philouze, C.; Del Valle, C. P.; Thomas, F. *Dalton Trans.* **2009**, 1792. (i) Shimazaki, Y.; Stack, T. D. P.; Storr, T. *Inorg. Chem.* **2009**, *48*, 8383. (j) Storr, T.; Verma, P.; Shimazaki, Y.; Wasinger, E. C.; Stack, T. D. P. *Chem. - Eur. J.* **2010**, *16*, 8980. (k) Kochem, A.; Orio, M.; Jarjayes, O.; Neese, F.; Thomas, F. *Chem. Commun.* **2010**, *46*, 6765. (l) Dunn, T. J.; Ramogida, C. F.; Simmonds, C.; Paterson, A.; Wong, E. W. Y.; Chiang, L.; Shimazaki, Y.; Storr, T. *Inorg. Chem.* **2011**, *50*, 6746. (m) Shimazaki, Y.; Arai, N.; Dunn, T. J.; Yajima, T.; Tani, F.; Ramogida, C. F.; Storr, T. *Dalton Trans.* **2011**, *40*, 2469. (n) Verma, P.; Pratt, R. C.; Storr, T.; Wasinger, E. C.; Stack, T. D. P. *Proc. Natl. Acad. Sci. U. S. A.* **2011**, *108*, 18600.

(8) (a) Pierpont, C. G.; Lange, C. W. *Prog. Inorg. Chem.* **1994**, *41*, 331. (b) Pierpont, C. G. *Inorg. Chem.* **2011**, *50*, 9766. (c) Verma, P.; Weir, J.; Mirica, L.; Stack, T. D. P. *Inorg. Chem.* **2011**, *50*, 9816.

(9) (a) Chaudhuri, P.; Verani, C. N.; Bill, E.; Bothe, E.; Weyhermüller, T.; Wieghardt, K. *J. Am. Chem. Soc.* **2001**, *123*, 2213. (b) Sun, X.; Chun, H.; Hildenbrand, K.; Bothe, E.; Weyhermüller, T.; Neese, F.; Wieghardt, K. *Inorg. Chem.* **2002**, *41*, 4295. (c) Smith, A. L.; Clapp, L. A.; Hardcastle, K. I.; Soper, J. D. *Polyhedron* **2010**, *29*, 164. (d) Smith, A. L.; Hardcastle, K. I.; Soper, J. D. *J. Am. Chem. Soc.* **2010**, *132*, 14358. (e) Dzik, W. I.; van der Vlugt, J. I.; Reek, J. N. H.; de Bruin, B. *Angew. Chem., Int. Ed.* **2011**, *50*, 3356. (f) Poddel'sky, A. I.; Cherkasov, V. K.; Abakumov, G. A. *Coord. Chem. Rev.* **2009**, *253*, 291. (g) Chaudhuri, P.; Hess, M.; Müller, J.; Hildenbrand, K.; Bill, E.; Weyhermüller, T.; Wieghardt, K. *J. Am. Chem. Soc.* **1999**, *121*, 9599. (h) Verani, C. N.; Gallert, S.; Bill, E.; Weyhermüller, T.; Wieghardt, K.; Chaudhuri, P. *Chem. Commun.* **1999**, 1747. (i) Chun, H.; Verani, C. N.; Chaudhuri, P.; Bothe, E.; Bill, E.; Weyhermüller, T.; Wieghardt, K. *Inorg. Chem.* **2001**, *40*, 4157. (j) Herebian, D.; Ghosh, P.; Chun, H.; Bothe, E.; Weyhermüller, T.; Wieghardt, K. *Eur. J. Inorg. Chem.* **2002**, *2002*, 1957. (k) Chun, H.; Chaudhuri, P.; Weyhermüller, T.; Wieghardt, K. *Inorg. Chem.* **2002**, *41*, 790. (l) Min, K. S.; Weyhermüller, T.; Wieghardt, K. *Dalton Trans.* **2003**, 1126. (m) Min, K. S.; Weyhermüller, T.; Bothe, E.; Wieghardt, K. *Inorg. Chem.* **2004**, *43*, 2922.

(10) (a) Ray, K.; Begum, A.; Weyhermüller, T.; Piligkos, S.; van Slageren, J.; Neese, F.; Wieghardt, K. *J. Am. Chem. Soc.* **2005**, *127*,

DOI: 10.1021/acs.inorgchem.5b01285
Inorg. Chem. 2015, 54, 9013−9026

4403. (b) Ray, K.; Petrenko, T.; Wieghardt, K.; Neese, F. *Dalton Trans.* **2007**, 1552. (c) Sproules, S.; Kapre, R. R.; Roy, N.; Weyhermüller, T.; Wieghardt, K. *Inorg. Chim. Acta* **2010**, *363*, 2702.
(11) (a) Caulton, K. G. *Eur. J. Inorg. Chem.* **2012**, *2012*, 435. (b) Hess, C. R.; Weyhermüller, T.; Bill, E.; Wieghardt, K. *Angew. Chem., Int. Ed.* **2009**, *48*, 3703. (c) Khusniyarov, M. M.; Weyhermüller, T.; Bill, E.; Wieghardt, K. *J. Am. Chem. Soc.* **2009**, *131*, 1208. (d) Muresan, N.; Chlopek, K.; Weyhermüller, T.; Neese, F.; Wieghardt, K. *Inorg. Chem.* **2007**, *46*, 5327. (e) de Bruin, B.; Bill, E.; Bothe, E.; Weyhermüller, T.; Wieghardt, K. *Inorg. Chem.* **2000**, *39*, 2936. (f) Bowman, A. C.; Milsmann, C.; Atienza, C. C. H.; Lobkovsky, E.; Wieghardt, K.; Chirik, P. J. *J. Am. Chem. Soc.* **2010**, *132*, 1676. (g) Darmon, J. M.; Stieber, S. C.; Sylvester, K. T.; Fernandez, I.; Lobkovsky, E.; Semproni, S. P.; Bill, E.; Wieghardt, K.; DeBEer, S.; Chirik, P. J. *J. Am. Chem. Soc.* **2012**, *134*, 17125. (h) Russell, S. K.; Bowman, A. C.; Lobkovsky, E.; Wieghardt, K.; Chirik, P. J. *Eur. J. Inorg. Chem.* **2012**, *2012*, 535.
(12) (a) Herebian, D.; Ghosh, P.; Chun, H.; Bothe, E.; Weyhermüller, T.; Wieghardt, K. *Eur. J. Inorg. Chem.* **2002**, *2002*, 1957. (b) Bill, E.; Bothe, E.; Chaudhuri, P.; Chlopek, C.; Herebian, D.; Kokatam, S.; Ray, K.; Weyhermüller, T.; Neese, F.; Wieghardt, K. *Chem. - Eur. J.* **2005**, *11*, 204.
(13) (a) Shimazaki, Y.; Tani, F.; Fukui, K.; Naruta, Y.; Yamauchi, O. *J. Am. Chem. Soc.* **2003**, *125*, 10512. (b) Storr, T.; Verma, P.; Pratt, R. C.; Wasinger, E. C.; Shimazaki, Y.; Stack, T. D. P. *J. Am. Chem. Soc.* **2008**, *130*, 15448.
(14) Orio, M.; Jarjayes, O.; Kanso, H.; Philouze, C.; Neese, F.; Thomas, F. *Angew. Chem., Int. Ed.* **2010**, *49*, 4989.
(15) Asami, K.; Tsukidate, K.; Iwatsuki, S.; Tani, F.; Karasawa, S.; Chiang, L.; Storr, T.; Thomas, F.; Shimazaki, Y. *Inorg. Chem.* **2012**, *51*, 12450.
(16) de Bellefeuille, D.; Askari, M. S.; Lassalle-Kaiser, B.; Journaux, Y.; Aukauloo, A.; Orio, M.; Thomas, F.; Ottenwaelder, X. *Inorg. Chem.* **2012**, *51*, 12796.
(17) Ottenwaelder, X.; Ruiz-Garcia, R.; Blondin, G.; Carasco, R.; Cano, J.; Lexa, D.; Journaux, Y.; Aukauloo, A. *Chem. Commun.* **2004**, 504.
(18) Ruiz, R.; Surville-Barland, C.; Aukauloo, A.; Anxolabehere-Mallart, E.; Journaux, Y.; Cano, J.; Muñoz, M. C. *J. Chem. Soc., Dalton Trans.* **1997**, 745.
(19) Barra, A. L.; Hassan, A. K.; Janoschka, A.; Schmidt, C. L.; Schünemann, V. *Appl. Magn. Reson.* **2006**, *30*, 385.
(20) Sheldrick, G. M. *SHELXL-97, Program for Crystal Structure Refinement*; University of Göttingen: Göttingen, Germany, 1997.
(21) Neese, F. *WIREs Comput. Mol. Sci.* **2012**, *2*, 73.
(22) Perdew, J. P. *Phys. Rev. B: Condens. Matter Mater. Phys.* **1986**, *33*, 8822.
(23) Perdew, J. P. *Phys. Rev. B: Condens. Matter Mater. Phys.* **1986**, *34*, 7406.
(24) Becke, A. D. *Phys. Rev. A: At., Mol., Opt. Phys.* **1988**, *38*, 3098.
(25) Schäfer, A.; Huber, C.; Ahlrichs, R. *J. Chem. Phys.* **1994**, *100*, 5829.
(26) Neese, F. *J. Comput. Chem.* **2003**, *24*, 1740.
(27) Weigend, F. *Phys. Chem. Chem. Phys.* **2006**, *8*, 1057.
(28) Klamt, A.; Schüürmann, G. *J. Chem. Soc., Perkin Trans. 2* **1993**, 799.
(29) Becke, A. D. *J. Chem. Phys.* **1993**, *98*, 1372.
(30) Lee, C. T.; Yang, W. T.; Parr, R. G. *Phys. Rev. B: Condens. Matter Mater. Phys.* **1988**, *37*, 785.
(31) Casida, M. E. *Recent Advances in Density Functional Methods*; Chong, D. P., Ed.; World Scientific: Singapore, 1995.
(32) Stratmann, R. E.; Scuseria, G. E.; Frisch, M. J. *J. Chem. Phys.* **1998**, *109*, 8218.
(33) Bauernschmitt, R.; Ahlrichs, R. *Chem. Phys. Lett.* **1996**, *256*, 454.
(34) Hirata, S.; Head-Gordon, M. *Chem. Phys. Lett.* **1999**, *314*, 291.
(35) Hirata, S.; Head-Gordon, M. *Chem. Phys. Lett.* **1999**, *302*, 375.
(36) Neese, F. *J. Chem. Phys.* **2001**, *115*, 11080.
(37) Koseki, S.; Schmidt, M. W.; Gordon, M. S. *J. Phys. Chem.* **1992**, *96*, 10768.
(38) Koseki, S.; Gordon, M. S.; Schmidt, M. W.; Matsunaga, N. *J. Phys. Chem.* **1995**, *99*, 12764.
(39) Neese, F. *J. Chem. Phys.* **2003**, *118*, 3939.
(40) Barone, V. *Recent Advances in Density Functional Methods*; Chong, D. P., Ed.; World Scientific: Singapore, 1996.
(41) Pantazis, D. A.; Chen, X.-Y.; Landis, C. R.; Neese, F. *J. Chem. Theory Comput.* **2008**, *4*, 908.
(42) Pantazis, D. A.; Neese, F. *J. Chem. Theory Comput.* **2009**, *5*, 2229.
(43) Noodleman, L.; Case, D. A. *Adv. Inorg. Chem.* **1992**, *38*, 423.
(44) Noodleman, L.; Davidson, E. R. *Chem. Phys.* **1986**, *109*, 131.
(45) Noodleman, L. *J. Chem. Phys.* **1981**, *74*, 5737.
(46) Soda, T.; Kitagawa, Y.; Onishi, T.; Takano, Y.; Shigeta, Y.; Nagao, H.; Yoshioka, Y.; Yamaguchi, K. *Chem. Phys. Lett.* **2000**, *319*, 223.
(47) Yamaguchi, K.; Takahara, Y.; Fueno, T. *Applied Quantum Chemistry V*; Smith, V. H., Ed.; Reidel: Dordrecht, The Netherlands, 1986.
(48) Heisenberg, W. *Eur. Phys. J. A* **1928**, *49*, 619.
(49) Heisenberg, W. *Eur. Phys. J. A* **1926**, *38*, 411.
(50) Dirac, P. a. M. *Proc. R. Soc. London, Ser. A* **1929**, *123*, 714.
(51) Van Vleck, J. H. *The Theory of Electronic and Magnetic Susceptibilities*; Oxford University: London, 1932.
(52) Ganyushin, D.; Neese, F. *J. Chem. Phys.* **2006**, *125*, 24103.
(53) (a) Thomas, F.; Jarjayes, O.; Duboc, C.; Philouze, C.; Saint-Aman, E.; Pierre, J.-L. *Dalton Trans.* **2004**, 2662. (b) Kochem, A.; Jarjayes, O.; Baptiste, B.; Philouze, C.; Vezin, H.; Tsukidate, K.; Tani, F.; Orio, M.; Shimazaki, Y.; Thomas, F. *Chem. - Eur. J.* **2012**, *18*, 1068. (c) Asami, K.; Takashina, A.; Kobayashi, M.; Iwatsuki, S.; Yajima, T.; Kochem, A.; van Gastel, M.; Tani, F.; Kohzuma, T.; Thomas, F.; Shimazaki, Y. *Dalton Trans.* **2014**, *43*, 2283.
(54) Cervera, B.; Sanz, J. L.; Ibáñez, M. J.; Vila, G.; Lloret, F.; Julve, M.; Ruiz, R.; Ottenwaelder, X.; Aukauloo, A.; Poussereau, S.; Journaux, Y.; Muñoz, M. C. *J. Chem. Soc., Dalton Trans.* **1998**, 781.
(55) Elbl-Weiser, K.; Krieger, C.; Staab, H. A. *Angew. Chem., Int. Ed. Engl.* **1990**, *29*, 211.
(56) Barth, T.; Krieger, C.; Neugebauer, F. A.; Staab, H. A. *Angew. Chem., Int. Ed. Engl.* **1991**, *30*, 1028.
(57) Elbl, K.; Krieger, C.; Staab, H. A. *Angew. Chem., Int. Ed. Engl.* **1986**, *25*, 1023.
(58) Barth, T.; Neugebauer, F. A. *J. Org. Chem.* **1995**, *60*, 5401.
(59) Michaelis, L.; Schubert, M. P.; Granick, S. *J. Am. Chem. Soc.* **1939**, *61*, 1981.
(60) Latta, B. M.; Taft, R. W. *J. Am. Chem. Soc.* **1967**, *89*, 5172.
(61) Klement, R.; Stock, F.; Elias, H.; Paulus, H.; Pelikán, P.; Valko, M.; Mazúr, M. *Polyhedron* **1999**, *18*, 3617.
(62) Yokoi, H.; Addison, A. W. *Inorg. Chem.* **1977**, *16*, 1341.
(63) Sakaguchi, U.; Addison, A. W. *J. Chem. Soc., Dalton Trans.* **1979**, 600.
(64) Allard, M. M.; Sonk, J. A.; Heeg, M. J.; McGarvey, B. R.; Schlegel, H. B.; Verani, C. *Angew. Chem., Int. Ed.* **2012**, *51*, 3178.
(65) Anson, F. C.; Collins, T. J.; Richmond, T. G.; Santarsiero, B. D.; Toth, J. E.; Treco, B. G. R. T. *J. Am. Chem. Soc.* **1987**, *109*, 2974.
(66) Bossu, F. P.; Chellappa, K. L.; Margerum, D. W. *J. Am. Chem. Soc.* **1977**, *99*, 2195.
(67) The nBu_4NPF_6 salt was prefered over nBu_4NClO_4 as the supporting electrolyte to generate $\mathbf{1}^+$ because it improves the separation of the first two redox processes and thus disfavors comproportionation of cation $\mathbf{1}^+$.
(68) Michel, F.; Thomas, F.; Hamman, S.; Philouze, C.; Saint-Aman, E.; Pierre, J.-L. *Eur. J. Inorg. Chem.* **2006**, *2006*, 3684.
(69) Benelli, C.; Gatteschi, D.; Zanchini, C.; Latour, J.-M.; Rey, P. *Inorg. Chem.* **1986**, *25*, 4242.
(70) (a) Shimazaki, Y.; Huth, S.; Hirota, S.; Yamauchi, O. *Bull. Chem. Soc. Jpn.* **2000**, *73*, 1187. (b) Philibert, A.; Thomas, F.; Philouze, C.; Hamman, S.; Saint- Aman, E.; Pierre, J.-L. *Chem. - Eur. J.* **2003**, *9*, 3803. (c) Michel, F.; Thomas, F.; Hamman, S.; Saint-Aman, E.; Bucher, C.; Pierre, J.-L. *Chem. - Eur. J.* **2004**, *10*, 4115.

DOI: 10.1021/acs.inorgchem.5b01285
Inorg. Chem. 2015, 54, 9013−9026

(71) Bencini, A.; Benelli, C.; Gatteschi, D.; Zanchini, C. *J. Am. Chem. Soc.* **1984**, *106*, 5813.
(72) (a) Pott, G. T.; Kommandeur, J. *J. Chem. Phys.* **1967**, *47*, 395. (b) Pott, G. T.; van Bruggen, C. F.; Kommandeur, J. *J. Chem. Phys.* **1967**, *47*, 408. (c) Metzger, R. M. *J. Chem. Phys.* **1976**, *64*, 2069.
(73) Veber, S. L.; Fedin, M. V.; Fokin, S. V.; Sagdeev, R. Z.; Ovcharenko, V. I.; Bagryanskaya, E. G. *Appl. Magn. Reson.* **2010**, *37*, 693.
(74) Complex $\mathbf{2}^{-}PPh_4^{+}$ dissolved in CH_2Cl_2 exhibits the same visible features as those of the electrochemically oxidized product. Complex $\mathbf{2}^{-}PPh_4^{+}$ was further characterized by IR spectroscopy (Figure S26). The change in the bonding pattern associated with quinoidal redistribution of the bond lengths was evidenced through shifts in the ring C−C and C−N vibrations (Sabitskii, A. V.; Kuznetsov, M. *J. Struct. Chem.* **1971**, *12*, 391). Its hygroscopic nature and instability did not allow us to characterize $\mathbf{2}^{-}PPh_4^{+}$ by elemental analysis.
(75) The magnetic properties of $\mathbf{1}^{+}$ and $\mathbf{2}^{-}$ were also investigated by DFT calculations. The calculated exchange-coupling constants J are +32 and +99 cm^{-1}, respectively, indicating that the two unpaired electrons are ferromagnetically coupled. This ferromagnetic coupling was expected from the orthogonality of the two magnetic orbitals. The calculated J values are, however, relatively weak, and distortions present in the solid state may lead to the antiferromagnetic exchange experimentally measured for $\mathbf{2}^{-}$.
(76) Bleaney, B.; Bowers, K. D. *Proc. R. Soc. London, Ser. A* **1952**, *214*, 451.
(77) Wang, Y.; DuBois, J. L.; Hedman, B.; Hodgson, K. O.; Stack, T. D. P. *Science* **1998**, *279*, 537.
(78) Sankar, M.; Nowicka, E.; Carter, E.; Murphy, D. M.; Knight, D. W.; Bethell, D.; Hutchings, G. J. *Nat. Commun.* **2014**, *5*, 3332.

DOI: 10.1021/acs.inorgchem.5b01285
Inorg. Chem. 2015, 54, 9013−9026